RESEARCH ARTICLE

Global Change Biology WILEY

Two sub-annual timescales and coupling modes for terrestrial water and carbon cycles

Daniel J. Short Gianotti[1] | Kaighin A. McColl[2,3] | Andrew F. Feldman[4,5] |
Xiangtao Xu[6] | Dara Entekhabi[1]

[1]Ralph M. Parsons Laboratory for Environmental Science and Engineering, Massachusetts Institute of Technology, Cambridge, Massachusetts, USA

[2]Department of Earth & Planetary Sciences, Harvard University, Cambridge, Massachusetts, USA

[3]John A Paulson School of Engineering & Applied Sciences, Harvard University, Cambridge, Massachusetts, USA

[4]Biospheric Sciences Laboratory, NASA Goddard Space Flight Center, Greenbelt, Maryland, USA

[5]Earth System Science Interdisciplinary Center, University of Maryland, Greenbelt, Maryland, USA

[6]Department of Ecology & Evolutionary Biology, Cornell University, Ithaca, New York, USA

Correspondence
Daniel J. Short Gianotti, Ralph M. Parsons Laboratory for Environmental Science and Engineering, Massachusetts Institute of Technology, Cambridge, MA, USA.
Email: gianotti@mit.edu

Abstract

To bridge the knowledge gap between (a) our (instantaneous-to-seasonal-scale) process understanding of plants and water and (b) our projections of long-term coupled feedbacks between the terrestrial water and carbon cycles, we must uncover what the dominant dynamics are linking fluxes of water and carbon. This study uses the simplest empirical dynamical systems models—two-dimensional linear models—and observation-based data from satellites, eddy covariance towers, weather stations, and machine-learning-derived products to determine the dominant sub-annual timescales coupling carbon uptake and (normalized) evaporation fluxes. We find two dominant modes across the Contiguous United States: (1) a negative correlation timescale on the order of a few days during which landscapes dry after precipitation and plants increase their carbon uptake through photosynthetic upregulation. (2) A slow, seasonal-scale positive covariation through which landscape drying leads to decreased growth and carbon uptake. The slow (positively correlated) process dominates the joint distribution of local water and carbon variables, leading to similar behaviors across space, biomes, and climate regions. We propose that vegetation cover/leaf area variables link this behavior across space, leading to strong emergent spatial patterns of water/carbon coupling in the mean. The spatial pattern of local temporal dynamics—positively sloped tangent lines to a convex long-term mean-state curve—is surprisingly strong, and can serve as a benchmark for coupled Earth System Models. We show that many such models do not represent this emergent mean-state pattern, and hypothesize that this may be due to lack of water-carbon feedbacks at daily scales.

KEYWORDS
attractor, carbon cycle, coupled, earth system model, emergent pattern, evaporation, feedbacks, flux tower, primary productivity, water cycle

1 | INTRODUCTION

The stability of ecosystems and local climates is controlled by two-way—or "coupled"—feedbacks between the water and carbon cycles (Green et al., 2017; Humphrey et al., 2021; Lemordant & Gentine, 2019; Sage, 2020; Yang et al., 2019). In one direction, water is a primary control on interannual carbon cycle variability (Piao, Wang, Wang, et al., 2020). Water controls ecosystem stress (Anderegg et al., 2015; Bartlett et al., 2016; Liu et al., 2020), productivity (Babst et al., 2019; Biederman et al., 2016; Feldman, Chulakadabba, et al., 2021; Peters et al., 2018; Post & Knapp, 2019; Scott et al., 2015), and biogeography (Babst et al., 2019; Jiao et al., 2021). In the other direction, terrestrial photosynthesis facilitates the diffusive and convective transfer of water and energy at the land-atmosphere interface (Green et al., 2017; Hong et al., 2019; Keenan & Williams, 2018; Knauer et al., 2017; Stoy et al., 2019; Ukkola et al., 2016).

While many questions about the future of the climate and ecosystems concern the coupled feedbacks between water and carbon on annual-to-century timescales, our mechanistic understanding of the governing processes is largely at the instantaneous-to-seasonal scales. Without proper understanding of how mechanistic dynamics scale to longer-term patterns and behaviors, it is not possible to constrain uncertainty or even develop basic intuition of longer-term projections of the Earth system.

The mechanisms linking the terrestrial water cycle and ecosystem carbon uptake (gross primary productivity [GPP]) depend on ecosystem structural dynamics (e.g., succession, growth, phenology, and mortality), vegetation physiology (e.g., chemical signaling, plant hydraulics, and stress responses), hydrogeography, biogeography, and atmospheric boundary layer gas and energy exchanges. These are difficult to represent in global models due to the substantial diversity of plant functions, traits, and responses to stress (D'Orangeville et al., 2018; dos Santos et al., 2021; Lavergne et al., 2019; Niinemets et al., 2015; Song et al., 2023). Because of this, it would be beneficial to establish simple benchmarks of the coupled water/carbon relationship which capture the dominant dynamics and co-variabilities of the two cycles.

We present one such benchmark, namely the dynamic feedbacks between landscape-integrated carbon uptake (GPP) and water fluxes. We specifically use the landscape evaporative fraction (EF $= \lambda E / [\lambda E + H]$, for latent heat flux λE and sensible heat flux H) as our water metric. The normalization of latent heat flux by available energy serves to remove many confounding effects of temperature and radiation differences across multiple sites. The terrestrial water cycle itself is tightly coupled so that water supply and demand can be nearly informationally indistinguishable (Gentine et al., 2007; McColl & Tang, 2023; Seneviratne et al., 2010). Because of this, EF is commonly used as both a metric of water availability and of land surface drying (Dirmeyer et al., 2000; Dong et al., 2022; Feldman et al., 2022). We will

explore the local temporal dynamics of GPP and EF using dynamical systems models—the simplest empirical representation of a bi-directional feedback system. We will specifically evaluate the dominant timescales of sub-annual water/carbon interactions in these ecosystems.

1.1 | Motivation

Before investigating the temporal dynamics of water and carbon interactions, we first examine the spatial mean patterns. Due to the high density of observational data, we will look across the bioclimatic gradients of the Contiguous United States (ConUS). Figure 1a,c,d shows the distribution of mean June–August (JJAS) $\overline{\text{GPP}}$ versus $\overline{\text{EF}}$ across ConUS from multiple data sets. Figure 1a shows GPP from the Moderate Resolution Imaging Spectroradiometer (MODIS) GPP product (MOD17A2) and EF calculated from meteorological variables using the "evapotranspiration based on equilibrated relative humidity" (ETRHEQ) method at 1798 weather stations across ConUS (data from Short Gianotti et al. (2019), and see methods). Because MODIS GPP is a modeled product—in particular, one which makes assumptions about the water cycle and water use efficiency—it is difficult to be certain that the relationship in Figure 1a is not imposed algorithmically. For comparison at the same sites, we show mean solar-induced fluorescence (SIF) data from the GOME-2 satellite versus station-derived EF in Figure 1b. Figure 1c shows mean JJAS GPP vs. EF from available ConUS eddy covariance flux towers, and 1d shows GPP vs. EF from the FluxCom machine-learning product trained on tower data and driven by meteorological and satellite observations. In all panels, we see a convex relationship between the photosynthetic metric on the y-axis and the mean EF across sites. The positive correlation is not surprising—locations with more available water can support more vegetation and will have higher evaporative fractions.

This study will tease apart the dynamic relationships between GPP and EF that lead to these averaged mean values. The questions we seek to answer here are (1) what are the dominant timescales of landscape dynamics coupling the water and carbon cycles, and (2) how are the water and carbon cycles linked on each of the timescales? In answering these questions, we hope to also explain how these patterns in the GPP-EF space arise.

2 | METHODS

To investigate the coupled water and carbon cycles, we focus primarily on two variables:

1. Gross primary productivity is the aggregate rate of carbon uptake from the atmosphere by landscape ecosystems. We use GPP measurements from multiple sources: eddy covariance
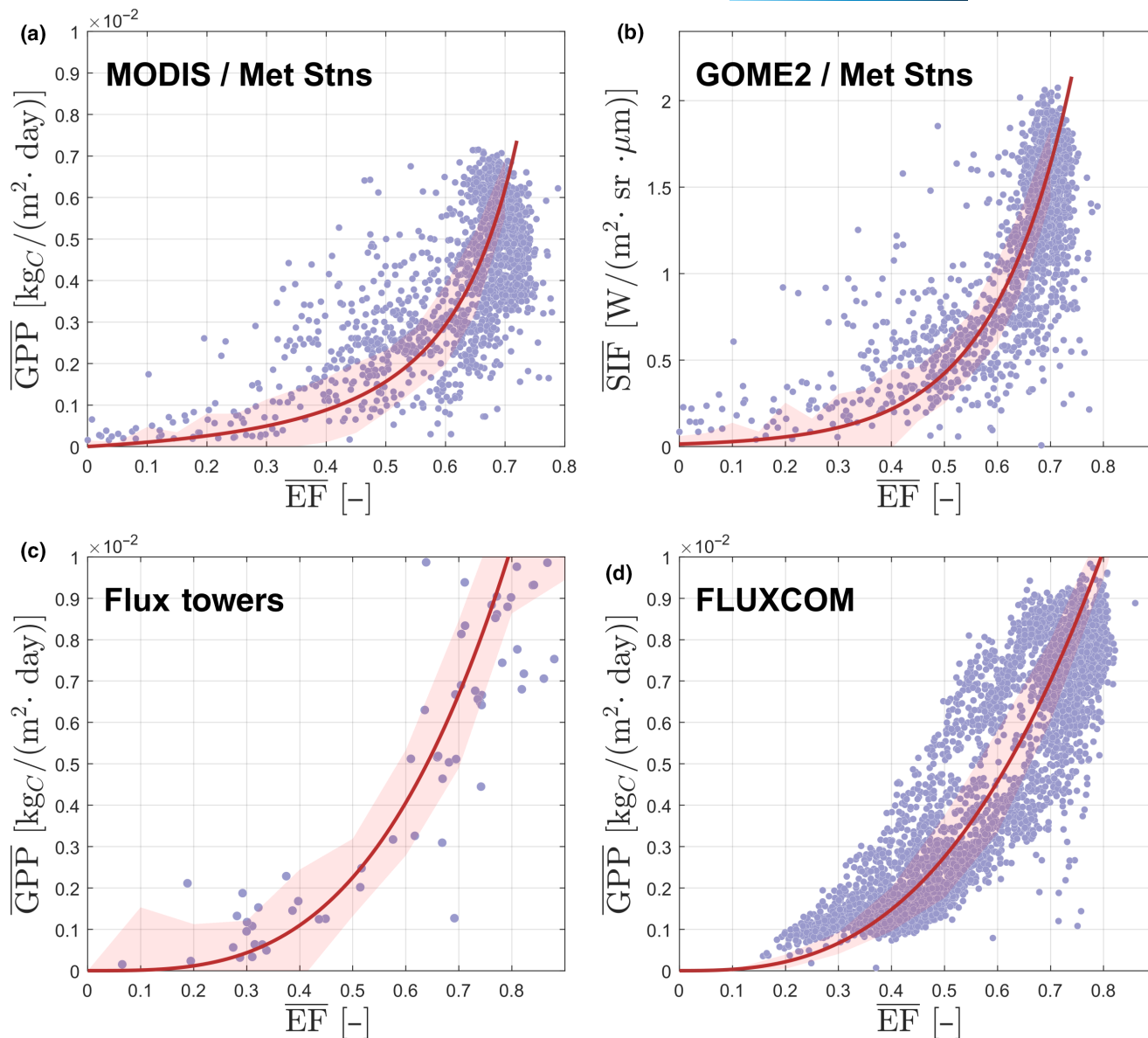
FIGURE 1 Relationship of time-averaged carbon and water variables across sites (biogeography). (a) Gross primary productivity (GPP) versus evaporative fraction (EF) at 1798 locations in the Contiguous United States (ConUS) (June–September). GPP estimated from MODIS sensor, and EF estimated from surface meteorological data using the ETRHEQ method (Rigden & Salvucci, 2015). The red line shows empirical curve fit and 99% confidence interval. (b) Same as (a) but using solar-induced fluorescence (SIF) from GOME-2 in place of MODIS GPP. At the large spatial scale, SIF covaries strongly with absorbed photosynthetically active radiation (APAR) as a photosynthetic proxy. (c) Same as (a), but with observations from ConUS eddy covariance flux towers. (d) Same as (a), but using output from the FLUXCOM. Both figures show a positively covarying, convex relationship across sites/bioclimate variability.

towers in the publicly available FLUXNET 2015 (Pastorello et al., 2020) and AmeriFlux (BASE and FLUXNET) datasets (Chu et al., 2023; Pastorello et al., 2020), satellite retrievals from the Moderate Resolution Imaging Spectroradiometer (Running et al., 2015), and estimates from the FluxCom machine-learning data set driven by eddy covariance and meteorological data (Jung et al., 2019; Tramontana et al., 2016). See Supplementary Table S2 for citations to individual eddy covariance datasets. We additionally use temporally averaged satellite-based SIF data from the GOME-2 instrument (Joiner et al., 2013) as a model-free proxy of satellite GPP.

2. Evaporative fraction (EF) is the fraction of turbulent energy flux at the land surface that goes to evaporating water:

$$\text{EF} = \frac{\lambda E}{\lambda E + H} \quad (1)$$

where λE is latent heat flux and H is sensible heat flux. EF is broadly monotonic with other water availability metrics (Haghighi et al., 2018; Short Gianotti et al., 2019) and normalizes latent heat flux to reduce confounding effects of surface energy budget terms—particularly the latitudinal gradient of mean incoming radiation, changing radiation conditions after rainfall, and mean temperatures.

2.1 | Spatial and temporal focus

All analyses are performed over the Contiguous 48 United States (ConUS) where the coverage densities of flux tower and weather stations are high.

For daily dynamics, we specifically look at interstorm periods ("drydowns"), during which there is no precipitation. Landscape state variables may have reliable state-dependent dynamics, but it is unlikely that the magnitudes and timings of exogenous precipitation events can be represented without full modeling of atmospheric circulation.

Daily data values are for the warm season with responsive vegetation (June 1–September 30) for all years used in each analysis.

Temporally averaged values for all variables are the average of daily values from June 1–September 30 for all years. Temporally averaged EF values are the ratio of the averaged numerator divided by the averaged denominator.

2.2 | Gridding the Drydowns in the GPP-EF space

Daily values of GPP, EF, and their first differences are used to fit linear dynamical system models to FLUXNET and FluxCom as shown in Figures 2–4 (see "Linear Dynamical Systems Model" section below). These models represent the daily dynamics (dEF/dt and dGPP/dt) as functions of the EF and GPP state variables. Because the ends of long drydowns tend to have a minimal dynamic range in GPP or EF, but with potentially many days of similar data, there is a tendency to oversample these drydown tails. To avoid associated biases (namely fitting primarily to the driest conditions, particularly in arid regions), we fit the dynamical system models to a gridded version of the daily data and first differences (see Figure 2). Gridded GPP and EF values are spaced evenly from zero to the maximum value observed at a site during all drydowns on a 17×17 grid (17 chosen as a subjective qualitative optimization, maximizing the number of observed gridded points with relatively few unobserved "holes" in the data range). For each of the gridded (EF, GPP) pairs, the first differences (temporal derivatives) are gridded using 2D natural neighbor interpolation. Grid boxes with no observations are not included. Examples of these gridded flow fields are shown in Figure 2 ("Gridded Flows"), and the linear models are fit to the gridded EF, GPP, dEF/dt, and dGPP/dt values.

2.3 | Joint density contours

The joint density contours shown in Figure 2 for specific drydown days are determined using all daily values 1, 3, 5, and 7 days after a precipitation event. To calculate the median contour (containing 50% of data) for Day 3, for example: (1) All GPP-EF pairs of the third day of all drydowns are selected. (2) A joint (2D) kernel density is fit to these pairs. (3) GPP-EF contours are numerically estimated at 250 evenly spaced density levels from 0 to the maximum

density. (4) The cumulative joint density is calculated numerically using the contour areas and level spacing. The smallest contour density is represented by a vertical cylindrical projection of the contour to the GPP-EF plane. The second smallest contour is a similar cylindrical projection, plus the volume of the smallest contour's layer, etc. (5) The "median contour" is that at which the cumulative joint density (volume) equals 0.5. The set of joint density contours shows the general progression of GPP and EF in the days following rain events.

2.4 | MODIS GPP

GPP from the MODIS MOD17A2 product, version 6 (Running et al., 2015), is used only in Figure 1a as averaged JJAS (June–September) values in comparison with contemporaneous EF values from USHCN/ETRHEQ (which is available only for Years 2015–2016), and are taken from Short Gianotti et al. (2019). 500m resolution 8-day composites are selected as the pixel containing the USHCN weather station. GPP values are averaged locally for all dates.

2.5 | GOME-2 SIF

Solar-induced fluorescence data are from the GOME-2 instrument on the MetOp-A satellite (Joiner et al., 2013). The data are nominally measured at 740nm with a spectral resolution of 0.5nm and a spatial resolution of 0.5°. All SIF values (including negative values) are averaged for JJAS days for a single mean value per pixel. We use the SIF data for local contemporaneous comparison with weather station-based EF values (USHCN/ETRHEQ, see below), and pair the weather station with the overlapping native pixel.

While chlorophyll fluorescence yields are often negatively correlated with carbon assimilation on the scale of a single leaf over seconds (e.g., sun flecks), fluorescence is positively correlated with absorbed photosynthetically active radiation (APAR) when aggregated in space and/or time (Jonard et al., 2020). SIF can thus be used an independent proxy for GPP at aggregated scales, with the benefit of no inherent assumptions about vegetation or water state (unlike satellite-derived GPP). SIF data are used only for Figure 1b.

2.6 | Flux towers

To show observed GPP-EF relationships and our methodological approach in Figure 2, we use daily GPP, latent heat fluxes, sensible heat fluxes, precipitation, and soil moisture data from three flux towers in the FLUXNET 2015 FULLSET data set (Pastorello et al., 2020): Willow Creek (US-WCr, JJAS 1999–2014) in northern Wisconsin (Cook et al., 2004), Metolius Young Pine Burn (US-Me6, JJAS 2010–2014) in western Oregon (Ruehr et al., 2012), and Santa Rita Grassland (US-SRG, JJAS 2008–2014) in southern Arizona (Scott et al., 2015).
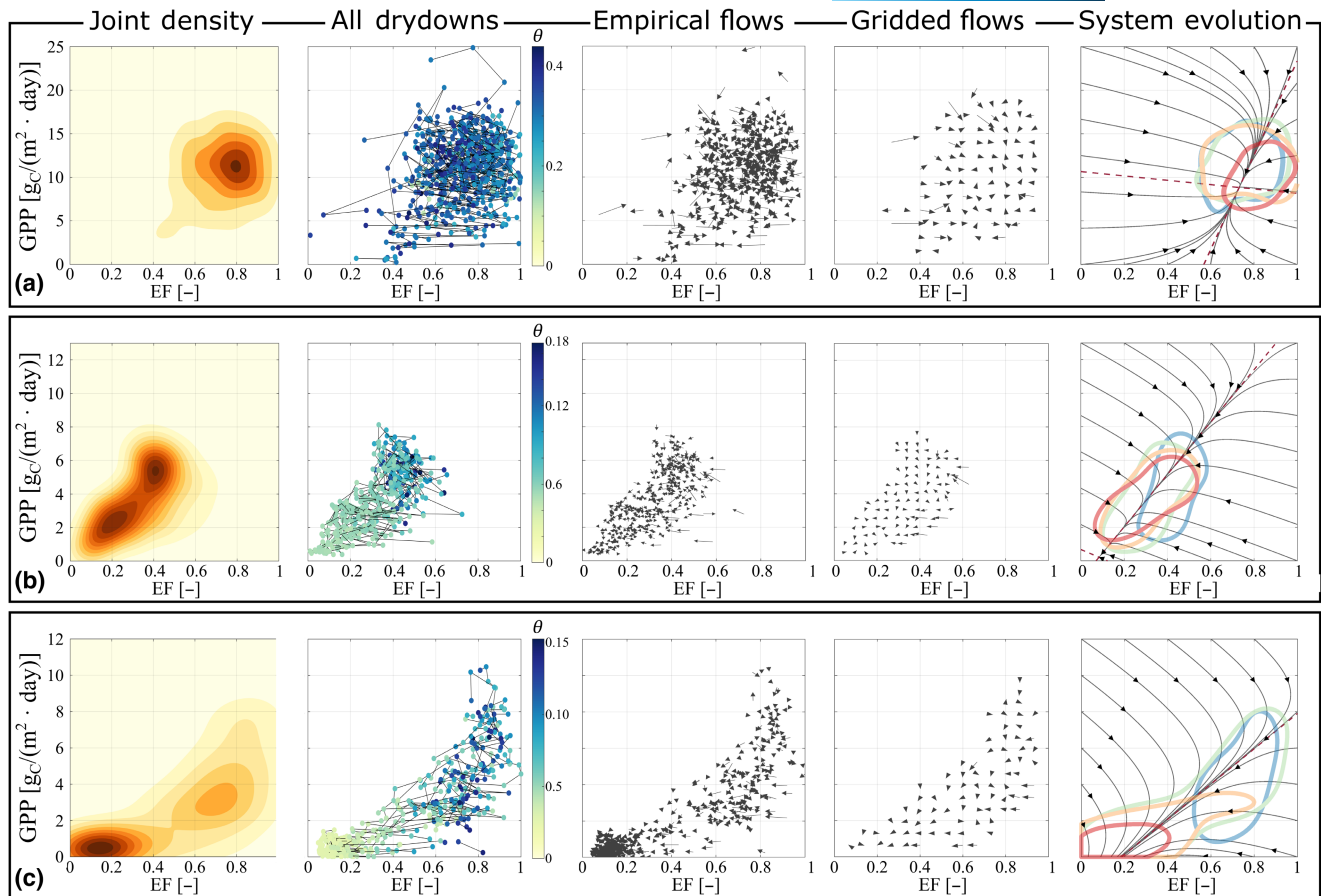
FIGURE 2 Daily-scale dynamics at three example flux towers across the humid to semi-arid axis. (a) Willow Creek (US-Wcr, DBF) in Wisconsin. (b) Metolius Young Pine Burn (US-Me6, ENF) in Oregon. (c) Santa Rita Grassland (US-SRG, GRA) in Arizona. Joint density is for all local daily JJAS data (including rainy days), all available years. Points in "All Drydowns" plots (first or left-most column) show daily (no rain) values colored by observed volumetric soil moisture θ at the tower site, and lines connect multi-day drydowns. Arrows in "Empirical Flows" plots (second column) show daily drydown progression. "Gridded Flows" plots (middle column) show gridded versions of the Empirical Flows. Arrows in "System Evolution" plots (last column) show fitted flowlines, red dashed lines show eigenvectors, colored contours show 90% probability density for GPP-EF pairs 1 day after rain (blue), 3 days (green), 5 days (orange) and 7 days (red). The "System Evolution" column shows that the dynamics is composed of a fast move to a sloped GPP-EF axis. The state of the system (typified by the progression of color contours) drifts over time along flowlines and eventually becomes the most probable state which is equivalent to the "All Drydowns" joint density (first column).

The GPP variable used for each site is GPP_DT_VUT_REF. The latent heat and sensible flux variables for each site are LE_F_MDS and H_F_MDS which are gap-filled using the MDS method. Soil moisture is SWC_F_MDS_1, using the uppermost soil layer. The precipitation variable is P_F, the consolidated site, and ERA precipitation variable. These data are used only in Figure 2.

Drydowns are determined as three or more consecutive days with zero reported precipitation.

Additionally, we use GPP (GPP_DT_VUT_REF) and EF (LE_F_MDS, H_F_MDS) data from all available ConUS sites for the long-term mean data shown in Figure 1c. Only sites with more than 8 months of JJAS data are shown, and sites classified as evergreen needle leaf, wetland, permanent snow or ice, barren, or urban are excluded. We use all sites with data available under the Creative Commons CC-BY-4.0 Data License, all of which are summarized and referenced in Table S2. Sites available in more than

one dataset are selected to use the dataset with the longest data record. Data are drawn from the FLUXNET 2015 data collection (Pastorello et al., 2020), the Ameriflux FLUXNET data collection (Pastorello et al., 2020), and the Ameriflux BASE data collection (Chu et al., 2023).

2.7 | FluxCom

Fluxes of surface sensible heat flux, latent heat flux, and GPP are used from the FluxCom machine-learning archive trained on eddy covariance tower data. We use all daily JJAS data from 1980 to 2013 at 0.5° resolution over ConUS. Carbon fluxes are from the CarbonFluxes version 1 dataset, "FluxCom (RS+METEO) Global Land Carbon Fluxes using CRUNCEP climate data" using the random forest method and CRUNCEP version 6 forcing (Jung, 2016; Jung

et al., 2020; Tramontana et al., 2016). GPP and respiration partitioning follow the method of Reichstein et al. (2012).

Latent and sensible heat fluxes are from the version 1 dataset, "FluxCom Global Land Energy Fluxes" (Jung, 2018; Jung et al., 2019; Tramontana et al., 2016). The turbulent fluxes are based on remotely sensed and meteorological data streams. The ensemble values are derived using all energy budget closure methods (Bowen ratio, residual method, and uncorrected) and all machine-learning methods (artificial neural network, multi-adaptive regression splines, and random forest) and are driven by the CRUNCEP version 6 climate data.

2.8 | ETRHEQ turbulent fluxes

Previous research has established and investigated an observed land—atmosphere coupling pattern—the minimization of the variance of the vertical relative humidity profile at the daily scale—which can be used to estimate surface conductances of moisture, sensible heat, and momentum (McColl & Rigden, 2020; Rigden & Salvucci, 2015; Salvucci & Gentine, 2013). These conductances can then be used to derive turbulent fluxes of sensible and latent heat from data available at surface meteorological stations, and finally EF through Equation 1. Turbulent fluxes have been validated against Flux Tower observations (Rigden & Salvucci, 2015, 2017). Using this method, EF was estimated previously at 1798 ConUS surface weather stations (Smith et al., 2011) in Short Gianotti et al. (2019). Daily turbulent flux data available from Short Gianotti et al. (2019), which span only the Years 2015–2016, are used here in Figure 1a,b. This temporal span determines the range MODIS GPP and GOME2 SIF data used as well. Because of the short temporal span of these EF data, we caution against using parameterized curve fits in Figure 1a,b alone for extrapolation. Fit curves are shown for qualitative comparison with independent data sources plotted in Figure 1c,d.

2.9 | CMIP6 data

To determine baseline coupling of the water and carbon cycles in models, we use data from the Coupled Model Intercomparison Project. We use the Pre-Industrial Control Run Earth System Model Experiment (esm-piControl, Figure 5). We additionally use data from the Historical Earth System Model Experiment (esm-hist) in Figure S3 to show the impact of land use harmonization on GPP-EF relationships. Data references for all CMIP6 data are in Table S1.

The esm-piControl experiment is designed to represent the period prior to the onset of large-scale industrialization (reference Year 1850), using a spin-up to allow the climate to come into balance with forcing (Eyring et al., 2016). Models all have dynamic carbon budgets, accounting for fluxes between the atmosphere, ocean, and biosphere.

For all experiments, model output is at the monthly scale. In Figure 5, pixel mean GPP is the mean of all monthly JJAS values. Pixel mean EF is the ratio of the mean of all monthly JJAS latent heat flux values to the mean of all JJAS latent plus sensible heat flux values.

2.10 | Data limitations

MODIS GPP is a modeled product based on assumptions about water use and vegetation class. This, of course, can lead to biases and artifacts. That said, MODIS GPP is entirely independent of the ETRHEQ fluxes, albeit with potential spatial representativeness issues between the two. Individual SIF retrievals from space have very low signal-to-noise ratios, but by aggregating in time, errors are greatly reduced (see Short Gianotti et al. (2019) for spatio-temporal relationships with water). The strong similarities between the two independent satellite products (MODIS GPP, GOME-2 SIF), and their further similarities with the longer duration Flux Tower and FluxCom data in Figure 1c,d in their relationships with EF, is evidence that the carbon–water relationship in Figure 1 is likely physical rather than artificial.

Flux towers are not common enough to represent the range of biomes and climates, even in the United States, but are benchmark references for local surface fluxes. FluxCom is based on the complex covariances of variables observed at flux towers, and relationships within the data can always potentially be driven by hard-wired mis-specification errors.

Any benchmark for physical models would ideally be determined using observations. The machine-learning algorithms used in estimating GPP and EF, while driven by meteorological and remotely sensed observations are of course statistical models themselves, which leaves opportunity for errors in process representation, just as physical models do. Despite this, the FluxCom data does not impose physical parameterizations (aside from energy balance corrections) that physical models a priori assume, which provides an independent estimation of daily- and seasonal-scale processes for comparison with other independent data sets. Additionally, the FluxCom data are trained on daily observations at eddy covariance sites specifically to optimize the representation of complex, non-linear responses of surface fluxes to meteorological forcing. These dynamics are then driven by observations, which we expect to empirically encode some of the physical processes captured by remote sensing (MODIS), flux towers, and meteorological data (CRUNCEP), including their biometeorological co-evolution at sub-seasonal scales. We suspect that the FluxCom data are the best available benchmarking tool for studying the co-evolution of land surface fluxes at continental scale without imposing that co-evolution structure physically. We also suspect that there will be errors in the extrapolation of statistical relationships to sites which are poorly represented by the FLUXNET training data, and so the parameters estimated from this data have high, and difficult to estimate uncertainties.
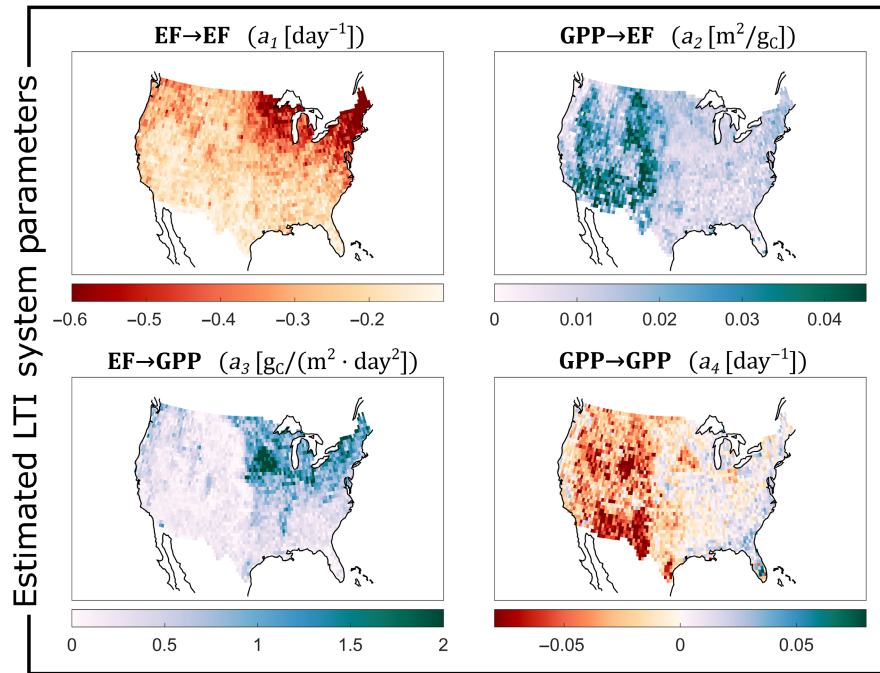
FIGURE 3 Empirical model parameters from daily JJAS FluxCom estimates. Parameters for the linear dynamical system model: $dEF/dt = a_1(EF - EF^\star) + a_2(GPP - GPP^\star)$ and $dGPP/dt = a_3(EF - EF^\star) + a_4(GPP - GPP^\star)$ (e.g., Equation 2). The parameters are estimated from daily gross primary productivity (GPP) and evaporative fraction (EF) values between rain events, as in Figure 2. The $EF \rightarrow EF$ notation highlights that (e.g.) parameter a_1 captures the feedbacks from the current EF value to the following day's EF value. Negative values suggest a negative feedback toward the intersection of the eigenvectors at $(EF^\star, GPP^\star)$. Positive values suggest a positive feedback—in this case, high EF values leading to EF increases for the next day and low EF values leading to further decreases in time (the latter being the typical drydown progression).

2.11 | Interstorm Drydowns

Drydowns for the fluxes associated with the FluxCom data are determined using the Climate Prediction Center's Unified Gauge-Based Analysis of Daily Precipitation over ConUS (CPCU) gridded precipitation data interpolated from daily station data (Chen et al., 2008). Individual drydowns are defined as three or more consecutive days with no precipitation reported. For compatibility with FluxCom data, all daily fluxes from the lower resolution (0.5°) FluxCom grid are matched with precipitation time series on the 0.25° precipitation CPCU grid (un-interpolated down-scaling). Fluxes occurring during identified drydowns from any CPCU pixel are then pooled and assigned back to the coarser-scale FluxCom grid so that GPP-EF co-evolutions during drydowns are represented according to the fraction of the pixel experiencing a drydown. All JJAS drydowns from 1980 to 2013 are included.

2.12 | Linear dynamical system model

We use a two-dimensional linear time-invariant (LTI) dynamical systems model for the analysis of first-order co-evolution between GPP and EF:

$$\frac{dEF}{dt} = a_1(EF - EF^\star) + a_2(GPP - GPP^\star) \tag{2a}$$

$$\frac{dGPP}{dt} = a_3(EF - EF^\star) + a_4(GPP - GPP^\star) \tag{2b}$$

where the parameters $EF^\star$ and $GPP^\star$ determine the fixed points of the system and a_1–a_4 are regression coefficients. This model treats the dynamics of GPP and EF as state-dependent so that changes in each variable in time are a function of the current GPP and EF states. Positive values of a_3, for example, suggest that higher EF values at a site are generally followed by an increase in GPP on the following day. This is the simplest state-dependent model of a coupled two-variable system, but can still yield somewhat complex distributions of the variables in time. We specifically apply this model only during drydown periods between rain events, as the dynamics of precipitation are radically different from those of the interstorm periods (both in terms of radiation and humidity gradients). Systems such as these are much simpler than non-linear dynamical models (such as the common Lotka-Volterra population model) or time-varying systems (where the a_1–a_4 parameters would change in time), and thus have a rich, well-established theoretical base. The system has two eigenvectors in the GPP-EF space, each with an associated eigenvalue (timescale). The eigenvectors cross at the point $(EF^\star, GPP^\star)$.

We fit the model at daily timestep to FLUXNET and FluxCom data, using only data within landscape drydowns between rain events of 3 days or more. These data and their first differences are gridded in the GPP-EF space (see above) and then used to
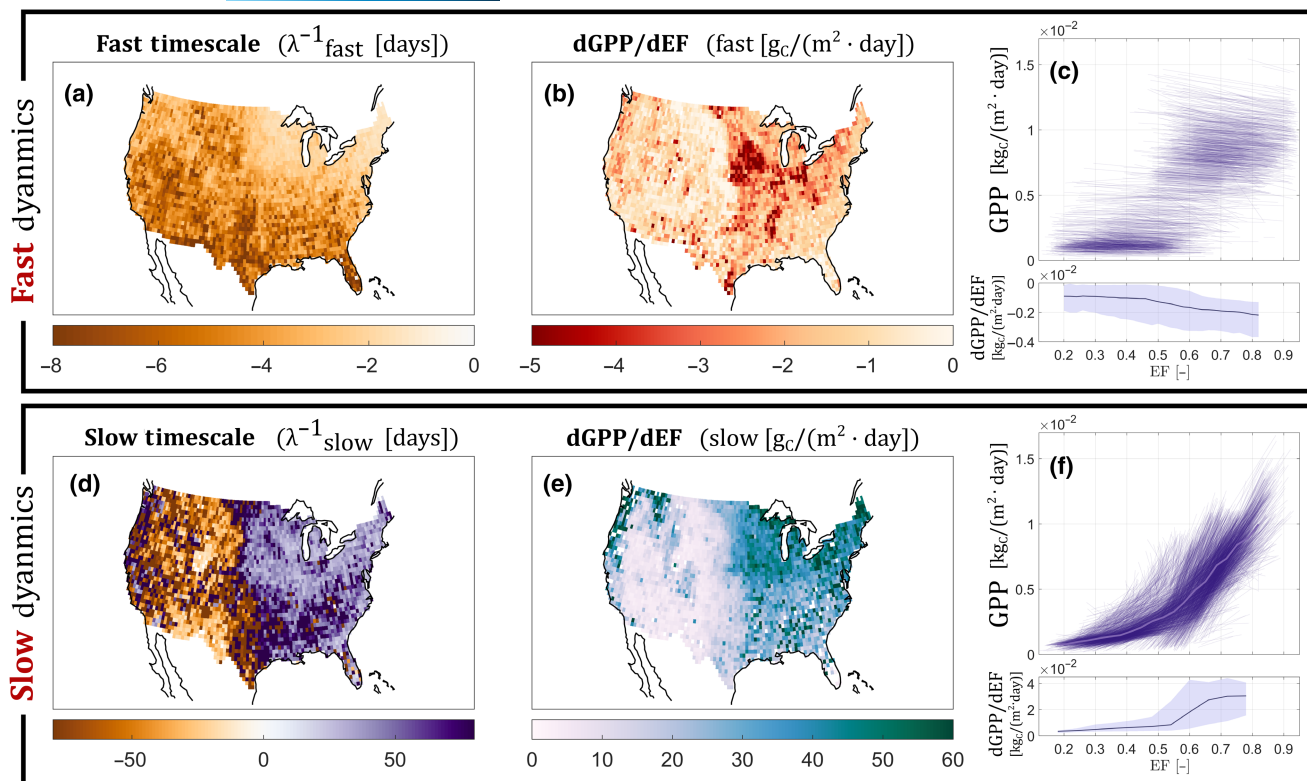
FIGURE 4 Fast and slow temporal dynamics of sub-seasonal GPP-EF co-evolution. (a) Timescale of fast dynamics using daily FluxCom JJAS GPP and EF and LTI model (Equation 1) after rain events; timescales are uniformly on the order of 1–8 days. (b) dGPP/dEF slope for fast dynamics during drydowns, negative (increasing Gross primary productivity [GPP] and decreasing evaporative fraction [EF]) across the Contiguous United States (ConUS). (c) Fast eigenvectors for every pixel in (a, b), with range equal to local quantiles 0.05–0.95 for all JJAS daily data. Slopes (lower panel) become more negative with increasing mean EF. (d–f) Same as (a–c) but for slow dynamics. Timescales (d) typically on the order of 30 days, timescale signs imply feedback class and separate water/energy limitation. Slopes are positive across ConUS and increase with mean EF. Light line in (f) shows mean values for all pixel eigenvectors in 25 uniform EF bins.

calculate maximum likelihood estimators of the system parameters. In each grid box, the EF, GPP, dEF/dt, and dGPP/dt values are calculated. Taken over all grid boxes, these data are used to estimate the parameters a_1, a_2, a_3, a_4, $EF^\star$, $GPP^\star$ at an individual site. Although these equations are linear in EF and GPP, they are not linear in the parameter space, so we use an unconstrained nonlinear optimization to minimize the squared (univariate Gaussian) errors of the dEF/dt and dGPP/dt values given the gridded EF and GPP values. This approach is similar to a weighted regression of the daily data with area-weighting—larger weights for individual observations in less-sampled areas and smaller weights in highly sampled areas.

Together, the system parameters (or equivalently, the eigenvalues and eigenvectors of $\begin{bmatrix} a_1 & a_2 \\ a_3 & a_4 \end{bmatrix}$), determine fast and slow system evolution. Combined with the system shocks (i.e., precipitation events), the system determination defines a joint distribution of EF and GPP (Brubaker & Entekhabi, 1996).

Eigenvector slopes can be written as

$$\frac{dGPP}{dEF} = \frac{\lambda - a_1}{a_2} = \frac{a_3}{\lambda - a_4} \qquad (3)$$

for the fast or slow eigenvectors associated with eigenvalue λ.

While linear models of GPP-EF dynamics can represent fairly complex behaviors (e.g., Figure 2), they are by construct simplistic. We select these models not because we believe dynamics are inherently linear, but because they allow us to summarize some basic properties of local water/carbon interactions—dominant timescales and slopes of interaction.

3 | RESULTS

3.1 | How do sub-seasonal dynamics drive the mean state?

The daily co-evolution of GPP and EF is subject to water availability shocks via rainfall. To uncover how local physical processes drive temporal dynamics, we examine the observed evolution of GPP-EF values across time at eddy covariance towers (Figure 2). The local joint distributions of daily GPP and EF are shown for three locations, with stronger temporal covariance shown in more water-limited, arid locations. The evolution of fluxes at a daily scale is shown during all drydowns after precipitation events, demonstrating a progression generally toward the higher density portions of the joint

FIGURE 5 Sample of Earth System Models from the CMIP6 esm-piControl experiment show a range of spatial covariance structures (biogeography), often misrepresenting the observed spatial relationship seen in Figures 1 and 4. Results in Figure 5 implicate the coupled relationship between biomass or leaf area and water availability metric evaporative fraction (EF).
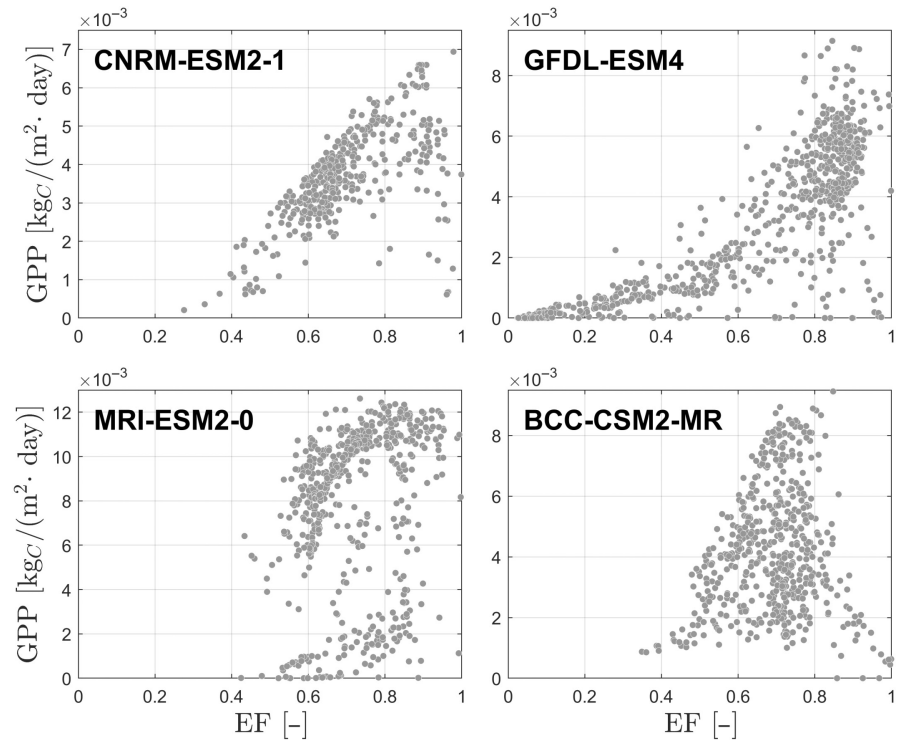
distributions, and a longer-term progression toward arid states (low EF and low GPP), particularly for the more arid locations.

To empirically evaluate the landscape response after a precipitation shock, we fit linear dynamical system models to gridded values of the daily-scale co-evolution of GPP and EF (Figure 2 "System Evolution"). These models are the simplest empirical fit of the flow field for the GPP-EF space.

The empirical dynamics in Figure 2 are represented by fast and slow eigenvectors, which establish the primary axes of within-drydown system evolution. The fast dynamics drive the GPP-EF state over the course of days toward the slow eigenvectors, which are also the areas of higher joint density. Within drydowns after rainfall, EF decreases, and GPP increases (negative covariation) until the water becomes limiting; then GPP falls in tandem with EF (Feldman et al., 2018, 2019; Feldman, Short Gianotti, et al., 2021). The landscape then follows the slow eigendirection on weekly-to-monthly scales, which determines the primary axis of water-carbon temporal coupling (now positive covariation), most dramatically in areas with less frequent rain. Note that the dGPP/dEF slope of the slow eigenvector is steepest in the wettest location and shallowest in the driest location. This holds broadly across ConUS flux towers (median fast/slow timescales: 2.4 days / 21.1 days) and corresponds to the geographical convexity of Figure 1.

3.2 | Fitting to FluxCom data

We perform the same analyses shown in Figure 2 to each pixel in the spatially gridded FluxCom dataset to determine model parameters for each location in ConUS. Figure 3 shows the estimated parameters for the model in Equation 2. Direct feedbacks from EF to itself (a_1) are always negative because the landscape is always drying between rain events. GPP feedbacks to EF (a_2) are positive as both photosynthetic upregulation and higher biomass correlate with higher transpiration. EF feedbacks to GPP (a_3) are positive due to both stomatal and growth responses to water availability (Claeys & Inzé, 2013). When GPP feedbacks to itself (a_4) are negative, this implies no water buffer for photosynthetic upregulation—the dominant stable state in this case is desiccation.

Figure 4a,b shows the timescales of the fast dynamics and the slopes of the corresponding eigenvectors from FluxCom data at each grid point. As with flux towers, the fast eigenvectors (median ConUS timescale 3.8 days) have negative slopes as EF decreases and GPP increases in the days immediately following rain. This demonstrates one basic hydrological-ecophysiological coupling mechanism: between storms, plants take up water and dry soils, allowing for rapid (e.g., stomatal, hormonal, growth acclimation, and turgor/osmotic adjustment) photosynthetic upregulation while water is sufficiently abundant (Claeys & Inzé, 2013; Feldman et al., 2018; Feldman, Short Gianotti, et al., 2021). This is a physiological response to pulses of water availability. A slope value of -1 $g_C/(m^2 \cdot day)$ can be directly interpreted as, for example, an increase in GPP of 0.1 $g_C/(m^2 \cdot day)$ as EF decreases by 0.1 in the first days after rainfall. Steeper slopes in irrigated regions suggest either highly water-sensitive vegetation or that changes in EF are due to exogenous covariates (e.g., harvest and accompanying end of irrigation).

3.3 | Local slow temporal dynamics are tangent to the geographic distribution

Slow dynamics (median ConUS timescale 33 days, Figure 4d,e) represent the sub-seasonal co-evolution of water and carbon fluxes, all with positive dGPP/dEF slopes. These positive slopes imply that the dominant local co-evolution of water and carbon fluxes is positively correlated and drives the positive covariance of the local joint GPP-EF densities (e.g. Figure 2 "Joint Density"). This is the long-term growth response and mode for EF-GPP coupling. Negative eigenvalues imply strong water limitation as for parameter a_4 in Figure 3.

The slow dGPP/dEF are more positive in more humid regions, and in particular increase with increasing climatological mean GPP and mean EF. This increasing local dGPP/dEF slope across geography—effectively an increasing normalized landscape WUE—implies that landscapes are more sensitive to changes in water availability in more humid regions. This is counter to the plant-level intuition of higher sensitivities in more arid conditions, but implicates total photosynthetic capacity (e.g., biomass and leaf area—positively correlated with water availability and transpiration) as the dominant driver of this coupling. Figure 4e is quite similar to maps of mean growing season leaf area index or vegetation density.

We note that the individual eigenvectors in Figure 4f are oriented along their own geographic distribution (convex curve). While local GPP-EF dynamics at monthly timescales need not be linear by any specific theory, the slow slopes are a best-linear approximation—effectively tangents to a convex spatial curve.

These paired emergent relationships in time and space suggest that the temporal dynamics of ecosystems (rather than a static biogeography) drive the mean-state water/carbon coupling seen in Figure 1 (see Figure S1 for direct comparison). It is known that phenology and sub-seasonal processes are critical in determining aggregate GPP (Pappas et al., 2017; Piao, Wang, Park, et al., 2020). Figure 4 suggests that sub-seasonal processes also drive the water–carbon feedbacks, in particular the landscape WUE represented by the slope of the curve.

Quantitatively, using the long-term mean curves of Figure 1 to estimate the slopes of the slow eigenvectors for daily FluxCom data in Figure 4f tend to slightly underestimate the slope (when evaluated across all FluxCom pixels, see Figure S2). Differences between using the curves from Figure 1a,c, or d are minimal.

3.4 | Earth system model performance

The spatial patterns depicted in Figure 1 can be thought of as space-for-time representations of GPP and EF dynamics at much longer timescales. To whatever extent diverse ecosystems couple GPP and EF along similar patterns, the mean states represent snapshots from a dynamic equilibrium of successionary, adaptive, growth-mortality, and climate coordination timescales. Mean states from networks of eddy covariance tower sites (not shown) show similar convex patterns to Figure 1, which lends support to the robustness of the emergent behavior.

For comparison with our observation-driven relationships, we show a sample of the same spatial relationship from ESMs from the CMIP6 esm-piControl experiment with no imposed land harmonization (Figure 5), which show diverse and diverging GPP/EF relationships (see Figure S3 for land use harmonization comparison). These relationships are not parameterized in models, but instead emerge from complex mechanistic representation of the coupled water and carbon cycles. Different models represent and include different physiological and ecological disturbance processes, but we would expect the spatial distribution of coupled water and carbon to show similar patterns to observations. Differences between the geography of modeled and observed GPP-EF imply that ecosystem water–carbon feedbacks may not be properly represented in some models, but the explanation for these mismatches is not yet mechanistically clear. Candidate mechanisms include growth and mortality dynamics (Anderegg et al., 2015), water/energy limitations on biomass production (Schwalm et al., 2017), differences in growth- and photosynthetic sensitivities to water state (Claeys & Inzé, 2013; Manandhar et al., 2017; Potkay & Feng, 2023), and temporal alignment of growing seasons with water availability and atmospheric water demand.

We highlight the GFDL-ESM4 model, which best captures the convex spatial pattern across ConUS in Figure 5. GFDL-ESM4 is one of only two ESMs (along with EC-Earth3) in the CMIP6 archive to represent dynamic ecosystem demography (Shevliakova et al., 2024). The other three models in Figure 5 do not represent sub-annual changes in vegetation type, nor do they represent sub-seasonal feedbacks from terrestrial water to daily plant dynamics. By comparison, the land surface model in GFDL-ESM4 represents multiple cohorts of vegetation per grid cell, each of which compete for water and energy resources at model timestep; and each cohort's leaf (LAI), wood (height), root, and sapwood carbon pools are updated daily in response to land surface conditions. This affects downstream vegetation cover fraction, albedo, and surface roughness, and allows vegetation dynamics to feed forward into the daily dynamics of the atmospheric boundary layer, including the water and energy cycles (Shevliakova et al., 2024). This does not conclusively prove that the coupling of water and carbon dynamics at the (ca. 3-day and ca. monthly) timescales we present here is the only driving force in the patterns of Figures 1, 5. It does however strongly suggest that inclusion of daily-to-monthly-scale feedbacks may be enough to push ESMs toward the observed relationships. GFDL-ESM4 does not have coupled nitrogen dynamics interacting with the terrestrial carbon model, suggesting that—at least over ConUS—water/carbon interactions (such as those in Figure 4f) may be the dominant drivers of the mean-state patterns in Figure 1.

A more complete interrogation of the role of dynamics versus static tuning parameters in ESMs would require analyses at daily output timescales, as opposed to the aggregated monthly values used in Figure 5.

4 | DISCUSSION

In both tower-based and FluxCom-based analyses, the coupling between water availability and carbon uptake is essentially always

negative (GPP increases as EF decreases) on daily timescales. The opposite is true at monthly timescales; GPP and EF are always positively coupled, and both decrease monotonically after rain. Broadly, we find that water–carbon dynamics change signs between short and long timescales. The difference in sign for the two sub-annual dynamics can be formalized in the eigenvector slopes in Figure 2, and Figure 4b,e. Fast processes with photosynthetic upregulation dominate on timescales of ca. 1–5 days; slow (ca. monthly) processes dominate beyond this, as landscape productivity rises and falls with available water. This behavior—switching from immediate negative correlation to positive correlation—has also previously been observed in entirely independent datasets of landscape vegetation water content and soil moisture (Feldman et al., 2018).

The general emergent convex patterns seen in Figure 1 can be understood from the slow dynamics as follows:

1. *The long-term mean values of GPP and EF are driven by slow (monthly scale) dynamics*. The slow eigenvectors represent the dominant GPP-EF conditions for ecosystems. The simple, empirical models quantify the dynamics of ecosystem behavior, namely the dynamic mean-state and responsiveness of the system to perturbations from that dynamic equilibrium (De Frenne et al., 2021; Shekhar et al., 2023). Following precipitation, ecosystems move rapidly (ca. 1–5 days) toward the slow eigenvector, and then, the variables co-evolve slowly in the slow eigenvalue direction (e.g., colored contours in Figure 2) with dGPP/dEF rates given by the slopes in Figure 4e. This pushes ecosystems' joint GPP-EF distributions toward the slow eigenvector, which serves as their main axes of dynamic equilibrium. The modes of ecosystem GPP-EF distributions should lie along or near their slow eigenvectors.

2. *Wetter locations have steeper dGPP/dEF slopes*. Somewhat counterintuitively, equivalent changes in EF correspond to larger GPP changes in humid ecosystems than in more arid ecosystems. While EF is also non-linearly related to more direct water supply metrics—such as volumetric soil moisture or soil saturation (Short Gianotti et al., 2019)—previous research suggests that evaporative metrics may be in some ways ideal for explaining water/carbon coupling relationships (Biederman et al., 2016; Franklin et al., 2020; Huxman et al., 2004; Knapp et al., 2017). Additionally, GPP itself is non-linearly related to direct soil water supply (Short Gianotti et al., 2019), and should vary to some degree with energy availability, which EF normalizes for.

3. *Slow dGPP/dEF slopes are controlled by biomass*. While we might think of arid regions having more sensitivity to water availability metrics than humid regions, the larger slopes in Figure 4 and the convexity of the spatial and temporal GPP-EF curves are more intuitive if we bear in mind that GPP is proportional to vegetation metrics such as above-ground biomass, vegetation cover fraction, or leaf area (LAI), simply through total landscape chlorophyll and APAR. A shock to the water availability in sparse desert may have large per-plant relative impacts, but will still lead to much smaller aggregate GPP change than a similar shock to a highly productive

forest. Still, it is not at all obvious that biomass state variables themselves are sufficiently sensitive to water availability so as to dominate the plant-level responses across plant functional types, photorespiratory pathways, and isohydricity (Claeys & Inzé, 2013; Manandhar et al., 2017; Pan et al., 2022; Schwalm et al., 2017). It does appear, however, that aggregate biomass metrics dominate the water/carbon coupling relationship at landscape scale (e.g., convex shapes of Figures 1, 4f, increasing slope with water availability in Figures 2, 4e,f. See also Figure S4).

4. *Steeper dGPP/dEF dynamic equilibria on monthly scales lead to the convex relationship across sites*. The effect of steeper dGPP/dEF relationships (slow eigenvector slopes, dominant axis of dynamic equilibrium) is that the mean values of GPP and EF fall along a convex, non-linear curve in Figure 1. The coherence of this shape across biomes and climate is surprising. The generality of this shape (and the co-alignment of the slow eigenvectors to form a similarly convex, coherent tangent bundle) suggests some near-equivalence of dynamics across vegetation biodiversity. Again, this is counterintuitive based on decades of study on the large range of plant sensitivities to water and strategies of water use, both across and within species (D'Orangeville et al., 2018; Lavergne et al., 2019; Niinemets et al., 2015; Song et al., 2023).

The role of biomass in this coupling provides a likely explanation, Laboratory experiments, and plant-scale optimality theories argue for increased plant water use efficiency in drier conditions pushing carbon–water correlation more toward negative; (Harrison et al., 2021; Katul et al., 2009; Lambers & Oliveira, 2019, pp. 60–64; Walker et al., 2020). Much of this is driven by sub-hourly stomatal responses and sub-daily photochemical regulation (Lambers & Oliveira, 2019; Schymanski et al., 2015). At the ecosystem scale, however, biomass increases with water availability (Franklin et al., 2020), along with the photosynthetic capacity of the landscape. This change in sign—akin to the changes in sign for dGPP/dEF at different timescales—shows the way in which carbon–water "optimization" is scale-dependent (Kull, 2002; Niu et al., 2011). We suggest that leaf-scale optimality drives ecosystems quickly (e.g., Figure 4c) to the slow (positively correlated) dynamic equilibrium of the landscape (e.g., Figure 4f)—governed by monthly growth, senescence, mortality, propagation, and disturbance response—which could be seen as its own landscape optimization of water and carbon (Anderegg et al., 2015; Richardson et al., 2013).

4.1 | Across-sites time-mean, local slow dynamics, and space-for-time substitutions

The spatial patterns in Figure 1 are qualitatively similar to the temporal patterns (across space) in Figure 4f. The curve traced out by the spatial ensemble of slow eigenvectors (Figure 4f) is an emergent behavior of the coupled water/carbon cycle dynamics. Individual slow eigenvectors look conspicuously like tangents to the spatial

pattern mapped out by the mean curve (Figure 4f) or the long-term mean values (Figure 1).

Although we do not have a theoretical model for a general (temporal and across-sites) relationship to explain all of the dynamics in Figure 4c,f, we speculate that the EF-GPP state of these landscapes move toward that spatial mean curve relatively quickly (ca. days) after rain events, with EF drying and GPP increasing. As they approach the mean curve, they dry more slowly along it with positive slope (EF still drying, but GPP decreasing) until another precipitation event disturbs the state evolution again. A general model could be very useful if it has predictive power for landscape evolution during interstorm periods and would be even more so with theoretical explanation. This could, in particular, be helpful in estimating the short-to-medium-term effects of landscape disturbances. We propose that these results could help land managers to establish likely behaviors of landscapes in response to changes in water regime or disturbances in above-ground biomass.

We hypothesize that local temporal land surface dynamics are tangent to the mean curve in Figures 1 and 4f whenever space-for-time substitutions are appropriate. This can only happen at the proper spatial and temporal scales. For example, on daily timescales all sites have dynamics somewhat orthogonal to that curve (Figure 4c). Similarly, sites recovering from major disturbance (e.g., deforestation) likely do not follow this coupling pattern because the water and carbon cycles become uncoupled until such point that recruitment, succession, and adaptation processes bring the system back to a new dynamic equilibrium. Additionally, space-for-time substitutions and the effects of aggregation scale are complicated by the role of Jensen's inequality, which requires that any non-linear relation cannot be equivalent across different transformations (e.g., spatial or temporal averaging) of the underlying variables. A fascinating question arises, whether there is a transformation of the water/carbon variables that is sufficiently linear to represent the dynamic equilibria across all time and spatial scales.

4.2 | Observational benchmark for earth system model emergent behaviors

The ESM data shown in Figure 5 (JJAS pixel means over ConUS) are intended to be compared with both the observational data in Figure 1 and the emergent spatial pattern from local temporal dynamics shown in Figure 4f. While some models show a general relationship between GPP and EF across space, the patterns shown are in some cases quite different from the convex shapes seen in Figures 1, 4. While some ESM experiments impose land use "harmonization" (prescribed land use pathways) to simplify intermodal comparison, we would expect any models with directly coupled carbon and water cycles to display similar emergent coupling patterns to observations. The fact that the models in Figure 5 do not all display these patterns suggests either mis-parameterization in the water and carbon cycles individually, or that fully coupled daily-to-monthly-scale dynamics between plants and water (e.g., response of

growth processes to water availability, transpiration dynamics, and magnitude of phenological variability) are necessary to get mean GPP and EF correct for the correct reasons.

Predictions of the global carbon and water budgets from Earth System Models in future climates—with different biodiversity, radiation, temperature, water availability, and carbon availability regimes—hinge on getting these feedbacks right. The dynamic vegetation models in the recent generation of ESMs parameterize both physiological and ecosystem structural dynamics, but may not fully represent structural response to water and heat stress (Allen et al., 2015; Anderegg et al., 2015; Brodribb et al., 2020; Fatichi et al., 2014; Peñuelas et al., 2017; Tei et al., 2017; Trugman et al., 2018).

We propose using the general emergent spatial patterns seen in this study to benchmark model output, at least for ConUS, but also likely more broadly across the mid-latitudes. It is also possible to run similar empirical dynamical analyses on daily ESM output, but spatial scaling effects—particularly Jensen's Inequality—would need to be dealt with carefully due to the non-linear relationships seen in Figures 1, 4 (Denny, 2017; Englund & Leonardsson, 2008).

4.3 | Water limitation definition

The negative a_4 values in Figure 3 and the negative eigenvalues in Figure 4 both seem to present a method for defining a kind of water limitation based on water–carbon coupling metrics (compare, e.g., with vegetation cover fraction in Figure S4 and traditional definitions of 100th parallel water limitation divides in Seager, Lis, et al. (2018)). Exactly how to interpret this definition is unclear, as is whether these forms of water limitation map onto the concept that landscapes may move in and out of water limitation over time (Akbar et al., 2019; Seager, Feldman, et al., 2018). While there is evidence that this aridity divide can be largely explained by water metrics alone (Seager, Lis, et al., 2018), water–vegetation interactions surely mediate the sub-seasonal dynamics through plant–water mechanisms, and thus mediate the long-term mean states and dynamics. Again, this is an area of ongoing and future research in the land surface processes community (Akbar et al., 2018; Denissen et al., 2020; Feldman et al., 2019; Fu et al., 2022; Zhang et al., 2016).

4.4 | Stomatal feedbacks muted at daily-averaged scale

Of the many coincident processes coupling the water and carbon cycles, one specific feedback that we do not see emerge in these analyses is the direct stomatal response on daily timescales. Specifically, one could expect that water availability promotes increases in stomatal conductance, increasing both carbon and water fluxes, leading to a positive GPP/EF correlation. Instead, we find that all estimated fast eigenvectors (Figure 4) have negative slopes, demonstrating that EF and GPP are still negatively correlated at these fast

timescales. This suggests that leaf area and upregulation dynamics dominate stomatal dynamics in this relationship at landscape scale (supported by isotopic studies; see Guerrieri et al., 2019; Mathias & Thomas, 2021), or that the impacts of stomatal response require observations at sub-daily timescales.

4.5 | Plant functions and traits

This approach is agnostic of vegetation classes, plant functional types, biome, and plant traits. Plants display incredible variability within and across species in linking water and carbon fluxes (Chaves et al., 2002). This specific framework appears to be fairly insensitive to across-landscape ecosystem functional differences—apart from how those functional differences collapse onto GPP/EF variables. We hypothesize that this implies that biomass/leaf area variables are the dominant drivers of this general pattern. Primary mechanisms that might drive plant-agnostic patterns include the tight coupling of water availability with surface conductance (including plant stomatal control, but particularly landscape stomatal density), rapid physiological shifts toward energy limitation in response to water inputs, and the scaling of T/ET ratios with biomass/leaf area.

The strength of the emergent relationships in this study reminds us that the water and carbon cycles are very tightly linked as has been demonstrated numerous times (Biederman et al., 2016; Huxman et al., 2004; Knapp et al., 2017; Short Gianotti et al., 2019). Hypotheses around this tight linkage form the basis for the entire sub-field of vegetation optimality theory (Eagleson & Tellers, 1982; Franklin et al., 2020; Fu et al., 2022; Mrad et al., 2019; Reynolds & Chen, 1996; Smith et al., 2019). In the case of this study, landscape coordination dynamics may be different from the effects of single-plant optimalities.

4.6 | Additional considerations

While we have included multiple datasets for these analyses, all have associated errors, which may be systematic. Further analyses at multiple spatial scales may help to clarify these relationships empirically and mechanistically.

When comparing the individual site dynamics in Figure 2 with the across all sites slow eigenvectors in Figure 4f, it seems clear that individual sites might follow a more non-linear dynamical system and that our linear model is overly simplistic. There is tower-based evidence for this at monthly scales (Short Gianotti & Entekhabi, 2024), but, to the best of our knowledge, no general mechanistic model. While the general pattern across sites seems likely to be mechanistically tied to the slope fields in Figure 4 (e.g., landscape water use efficiency and light use efficiency), it is difficult to design a purely empirical model to represent the full behavior of a general dynamical system for all sites without being over-parameterized. This may be an area of further investigation, particularly using dominant physical

dynamics along with some degree of empiricism to represent general GPP-EF patterns.

5 | CONCLUSIONS

We see a positively covarying, convex relationship between landscape-level carbon and water fluxes. This appears in both (1) across-site time means and (2) single-site sub-annual temporal dynamics. This pattern emerges in multiple independent datasets, including remotely sensed GPP proxies paired with surface meteorological observations (Figure 1); individual flux towers (Figures 1, 2); and machine-learning-based, observationally driven data (Figures 1, 4).

After rain events, across datasets, we see that landscapes dry and increase their carbon uptake rate (negative correlation) for days, and then switch to a dominant, slow relationship with timescales of weeks to months. On these slower timescales, GPP and EF become positively correlated; sufficient drying without precipitation leads to drought and loss of local carbon sink.

More humid locations have steeper slow GPP-EF slopes, as an equivalent loss of moisture in a verdant location leads to a larger absolute loss of biomass or photosynthetic capacity than in a scarcely vegetated landscape.

While the spatial and temporal patterns are emergent, an intuitive, hypothetical pathway is that excess water availability at the landscape-level spurs increasing leaf allocation to reduce light limitation. This could be at the plant level, or simply at the scale of landscape growth and reproductive success. Increased photosynthetic capacity in turn increases GPP and transpiration, decreasing water availability.

We hypothesize that this relationship may be radically different for sites experiencing major disturbance events (Brodribb et al., 2020; Peterson et al., 2021). Even if there are generalizable processes stabilizing carbon/water dynamics at sub-seasonal timescales, they might or might not remain coupled on the successional and coordination timescales that control biogeography. At the proper time and disturbance scales, however, the relationships shown in this study could help to guide projections of natural and managed ecosystem behavior, and the response of landscapes to management practices and climate change mitigation actions.

Many Earth System Models fail to capture the observed spatial patterns, likely due to insufficient coupling schemes between growth, phenology, water availability, and evapotranspiration. This implies underlying problems in mechanistic representation of the terrestrial water and carbon cycles, which could significantly impact the results of carbon, water, and energy budgets in forward runs of individual models and the CMIP6 ensemble.

At the basic science level, it is empirically tempting to view Figure 4f as a non-linear attractor over which diverse landscapes appear to evolve. Minor disturbance—including individual rain events—pushes sites away from this curve; they move back toward the curve over days, and then perhaps trace its path slowly until

the next rain event. This is a very simple representation of the integrated effects of many complex processes which we currently struggle to capture at large scales. A theoretically derived explanation for these empirical patterns—if indeed they hold—would greatly assist in constraining global water–carbon feedbacks in models and forecasts, as well as our understanding of the stability of the broader Earth System.

AUTHOR CONTRIBUTIONS

Daniel J. Short Gianotti: Conceptualization; data curation; formal analysis; investigation; methodology; project administration; validation; visualization; writing – original draft; writing – review and editing. **Dara Entekhabi:** Conceptualization; methodology; project administration; resources; supervision; writing – review and editing. **Kaighin A. McColl:** Methodology; writing – review and editing. **Andrew F. Feldman:** Methodology; writing – review and editing. **Xiangtao Xu:** Methodology; writing – review and editing.

FUNDING INFORMATION

CONFLICT OF INTEREST STATEMENT

The authors have no conflict of interest to declare.

DATA AVAILABILITY STATEMENT

The data that support the findings of this study and that are used to generate the included figures are openly available in Zenodo repository 13,144,427 (Short Gianotti, 2024) at https://doi.org/10.5281/zenodo.13144427. These data were derived from the following resources, all in the public domain. Gridded precipitation data from the Climate Prediction Center are available through the CPC FTP server (ftp://ftp.cpc.ncep.noaa.gov/precip/CPC_UNI_PRCP/GAUGE_CONUS/). FluxCom data are available from the FluxCom initiative (http://www.fluxcom.org) from the data portal of the Max Plank Institute for Biogeochemistry (https://www.bgc-jena.mpg.de/geodb/projects/Home.php). MODIS GPP, LAI, and landcover data are available from the NASA EOSDIS Land Processes DAAC (https://lpdaac.usgs.gov). GOME-2 SIF data are available NASA Goddard Space Flight Center (https://avdc.gsfc.nasa.gov/pub/data/satellite/MetOp/GOME_F/). Weather station data driving the ETRHEQ method are available from the National Centers for Environmental Information (https://www.ncei.noaa.gov/access/search/data-search/global-hourly). MERRA-2 radiation data are available from the Goddard Earth Sciences Data and Information Services Center portal (https://disc.gsfc.nasa.gov/). CMIP 6 model output are available from the World Climate Research Program Earth System Grid Federation portal (https://esgf-node.llnl.gov/projects/cmip6/). Eddy covariance data are available from FLUXNET (https://fluxnet.org/data/fluxnet2015-dataset/), and AmeriFlux (https://ameriflux.lbl.gov/data/flux-data-products/). Individual DOIs for every eddy covariance site's data are listed in full in Supplemental Table S2. SMAP soil moisture data are available from the National Snow and Ice Data Center (https://nsidc.org/data/smap/smap-data.html).

ORCID

Daniel J. Short Gianotti https://orcid.org/0000-0003-4891-2474
Kaighin A. McColl https://orcid.org/0000-0001-9201-6760
Andrew F. Feldman https://orcid.org/0000-0003-1547-6995
Xiangtao Xu https://orcid.org/0000-0002-9402-9474
Dara Entekhabi https://orcid.org/0000-0002-8362-4761

REFERENCES

Akbar, R., Short, D. J., Gianotti, K. A. M., Haghighi, E., Salvucci, G. D., Entekhabi, D., Short Gianotti, D. J., McColl, K. A., Haghighi, E., Salvucci, G. D., & Entekhabi, D. (2018). Estimation of landscape soil water losses from satellite observations of soil moisture. *Journal of Hydrometeorology*, 19(5), 871–889. https://doi.org/10.1175/JHM-D-17-0200.1

Akbar, R., Short Gianotti, D. J., Salvucci, G. D., & Entekhabi, D. (2019). Mapped hydroclimatology of evapotranspiration and drainage runoff using SMAP brightness temperature observations and precipitation Information. *Water Resources Research*, 55, 3391–3413. https://doi.org/10.1029/2018WR024459

Allen, C. D., Breshears, D. D., Mcdowell, N. G., Allen, C., Breshears, D. D., & Mcdowell, N. G. (2015). On underestimation of global vulnerability to tree mortality and forest die-off from hotter drought in the Anthropocene. *Ecosphere*, 6(8), 1–55. https://doi.org/10.1890/ES15-00203.1

Anderegg, W. R. L., Schwalm, C., Biondi, F., Camarero, J. J., Koch, G., Litvak, M., Ogle, K., Shaw, J. D., Shevliakova, E., Williams, A. P., Wolf, A., Ziaco, E., & Pacala, S. (2015). Pervasive drought legacies in forest ecosystems and their implications for carbon cycle models. *Science*, 349(6247), 528–532. https://doi.org/10.1126/science.aab1833

Babst, F., Bouriaud, O., Poulter, B., Trouet, V., Girardin, M. P., & Frank, D. C. (2019). Twentieth century redistribution in climatic drivers of global tree growth. *Science Advances*, 5(1), 1–10. https://doi.org/10.1126/sciadv.aat4313

Bartlett, M. K., Klein, T., Jansen, S., Choat, B., & Sack, L. (2016). The correlations and sequence of plant stomatal, hydraulic, and wilting responses to drought. *Proceedings of the National Academy of Sciences*, 113(46), 13098–13103. https://doi.org/10.1073/pnas.1604088113

Biederman, J. A., Scott, R. L., Goulden, M. L., Vargas, R., Litvak, M. E., Kolb, T. E., Yepez, E. A., Oechel, W. C., Blanken, P. D., Bell, T. W., Garatuza-Payan, J., Maurer, G. E., Dore, S., & Burns, S. P. (2016). Terrestrial carbon balance in a drier world: The effects of water availability in southwestern North America. *Global Change Biology*, 22(5), 1867–1879. https://doi.org/10.1111/gcb.13222

Brodribb, T. J., Powers, J., Cochard, H., & Choat, B. (2020). Hanging by a thread? Forests and drought. *Science*, 368(6488), 261–266. https://doi.org/10.1126/science.aat7631

Brubaker, K. L., & Entekhabi, D. (1996). Analysis of feedback mechanisms in land-atmosphere interaction. *Water Resources Research*, 32(5), 1343–1357. https://doi.org/10.1029/96WR00005

Chaves, M. M., Pereira, J. S., Maroco, J., Rodrigues, M. L., Ricardo, C. P. P., Osório, M. L., Carvalho, I., Faria, T., & Pinheiro, C. (2002). How plants cope with water stress in the field? Photosynthesis and Growth. *Annals of Botany*, 89(7), 907–916. https://doi.org/10.1093/AOB/MCF105

Chen, M., Shi, W., Xie, P., Silva, V. B. S. S., Kousky, V. E., Higgins, R. W., & Janowiak, J. E. (2008). Assessing objective techniques for gauge-based analyses of global daily precipitation. *Journal of Geophysical*

Research-Atmospheres, 113(4), 1–13. https://doi.org/10.1029/2007JD009132

Chu, H., Christianson, D. S., Cheah, Y. W., Pastorello, G., O'Brien, F., Geden, J., Ngo, S. T., Hollowgrass, R., Leibowitz, K., Beekwilder, N. F., Sandesh, M., Dengel, S., Chan, S. W., Santos, A., Delwiche, K., Yi, K., Buechner, C., Baldocchi, D., Papale, D., ... Torn, M. S. (2023). AmeriFlux BASE data pipeline to support network growth and data sharing. *Scientific Data*, 10(1), 1–13. https://doi.org/10.1038/s41597-023-02531-2

Claeys, H., & Inzé, D. (2013). The agony of choice: How plants balance growth and survival under water-limiting conditions. *Plant Physiology*, 162(4), 1768–1779. https://doi.org/10.1104/PP.113.220921

Cook, B. D., Davis, K. J., Wang, W., Desai, A., Berger, B. W., Teclaw, R. M., Martin, J. G., Bolstad, P. V., Bakwin, P. S., Yi, C., & Heilman, W. (2004). Carbon exchange and venting anomalies in an upland deciduous forest in northern Wisconsin, USA. *Agricultural and Forest Meteorology*, 126(3–4), 271–295. https://doi.org/10.1016/J.AGRFORMET.2004.06.008

De Frenne, P., Lenoir, J., Luoto, M., Scheffers, B. R., Zellweger, F., Aalto, J., Ashcroft, M. B., Christiansen, D. M., Decocq, G., De Pauw, K., Govaert, S., Greiser, C., Gril, E., Hampe, A., Jucker, T., Klinges, D. H., Koelemeijer, I. A., Lembrechts, J. J., Marrec, R., ... Hylander, K. (2021). Forest microclimates and climate change: Importance, drivers and future research agenda. *Global Change Biology*, 27(11), 2279–2297. https://doi.org/10.1111/GCB.15569

Denissen, J. M. C., Teuling, A. J., Reichstein, M., & Orth, R. (2020). Critical soil moisture derived from satellite observations over Europe. *Journal of Geophysical Research: Atmospheres*, 125(6), e2019JD031672. https://doi.org/10.1029/2019JD031672

Denny, M. (2017). The fallacy of the average: On the ubiquity, utility and continuing novelty of Jensen's inequality. *Journal of Experimental Biology*, 220(2), 139–146. https://doi.org/10.1242/JEB.140368

Dirmeyer, P. A., Zeng, F. J., Ducharne, A., Morrill, J. C., Koster, R. D., Dirmeyer, P. A., Zeng, F. J., Ducharne, A., Morrill, J. C., & Koster, R. D. (2000). The sensitivity of surface fluxes to soil water content in three land surface schemes. *Journal of Hydrometeorology*, 1(2), 121–134. https://doi.org/10.1175/1525-7541(2000)001<0121:TSOSFT>2.0.CO;2

Dong, J., Akbar, R., Short Gianotti, D. J., Feldman, A. F., Crow, W. T., & Entekhabi, D. (2022). Can surface soil moisture Information identify evapotranspiration regime transitions? *Geophysical Research Letters*, 49(7), e2021GL097697. https://doi.org/10.1029/2021GL097697

D'Orangeville, L., Maxwell, J., Kneeshaw, D., Pederson, N., Duchesne, L., Logan, T., Houle, D., Arseneault, D., Beier, C. M., Bishop, D. A., Druckenbrod, D., Fraver, S., Girard, F., Halman, J., Hansen, C., Hart, J. L., Hartmann, H., Kaye, M., Leblanc, D., ... Phillips, R. P. (2018). Drought timing and local climate determine the sensitivity of eastern temperate forests to drought. *Global Change Biology*, 24(6), 2339–2351. https://doi.org/10.1111/GCB.14096

dos Santos, T., Keppel-Aleks, G., De Roo, R., & Steiner, A. L. (2021). Can land surface models capture the observed soil moisture control of water and carbon fluxes in temperate-to-boreal forests? *Journal of Geophysical Research: Biogeosciences*, 126(4), e2020JG005999. https://doi.org/10.1029/2020JG005999

Eagleson, P. S., & Tellers, T. E. (1982). Ecological optimality in water-limited soil-vegetation systems 2. Tests and applications. *Water Resources Research*, 18(2), 341–354. https://doi.org/10.1029/WR018i002p00341

Englund, G., & Leonardsson, K. (2008). Scaling up the functional response for spatially heterogeneous systems. *Ecology Letters*, 11(5), 440–449. https://doi.org/10.1111/J.1461-0248.2008.01159.X

Eyring, V., Bony, S., Meehl, G. A., Senior, C. A., Stevens, B., Stouffer, R. J., & Taylor, K. E. (2016). Overview of the coupled model intercomparison project phase 6 (CMIP6) experimental design and organization. *Geoscientific Model Development*, 9, 1937–1958. https://doi.org/10.5194/gmd-9-1937-2016

Fatichi, S., Leuzinger, S., & Körner, C. (2014). Moving beyond photosynthesis: From carbon source to sink-driven vegetation modeling. *New Phytologist*, 201(4), 1086–1095. https://doi.org/10.1111/NPH.12614

Feldman, A. F., Chulakadabba, A., Short Gianotti, D. J., & Entekhabi, D. (2021). Landscape-scale plant water content and carbon flux behavior following moisture pulses: From dryland to mesic environments. *Water Resources Research*, 57(1), 1–20. https://doi.org/10.1029/2020WR027592

Feldman, A. F., Short Gianotti, D. J., Konings, A. G., Gentine, P., & Entekhabi, D. (2021). Patterns of plant rehydration and growth following pulses of soil moisture availability. *Biogeosciences*, 18(3), 831–847. https://doi.org/10.5194/BG-18-831-2021

Feldman, A. F., Short Gianotti, D. J., Konings, A. G., McColl, K. A., Akbar, R., Salvucci, G. D., & Entekhabi, D. (2018). Moisture pulse-reserve in the soil-plant continuum observed across biomes. *Nature Plants*, 4(12), 1026–1033. https://doi.org/10.1038/s41477-018-0304-9

Feldman, A. F., Short Gianotti, D. J., Trigo, I. F., Salvucci, G. D., & Entekhabi, D. (2019). Satellite-based assessment of land surface energy partitioning–soil moisture relationships and effects of confounding variables. *Water Resources Research*, 55(12), 10657–10677. https://doi.org/10.1029/2019WR025874

Feldman, A. F., Short Gianotti, D. J., Trigo, I. F., Salvucci, G. D., & Entekhabi, D. (2022). Observed landscape responsiveness to climate forcing. *Water Resources Research*, 58(1), e2021WR030316. https://doi.org/10.1029/2021WR030316

Franklin, O., Harrison, S. P., Dewar, R., Farrior, C. E., Brännström, Å., Dieckmann, U., Pietsch, S., Falster, D., Cramer, W., Loreau, M., Wang, H., Mäkelä, A., Rebel, K. T., Meron, E., Schymanski, S. J., Rovenskaya, E., Stocker, B. D., Zaehle, S., Manzoni, S., ... Prentice, I. C. (2020). Organizing principles for vegetation dynamics. *Nature Plants*, 6(5), 444–453. https://doi.org/10.1038/s41477-020-0655-x

Fu, Z., Ciais, P., Feldman, A. F., Gentine, P., Makowski, D., Prentice, I. C., Stoy, P. C., Bastos, A., & Wigneron, J. P. (2022). Critical soil moisture thresholds of plant water stress in terrestrial ecosystems. *Science Advances*, 8(44), 7827. https://doi.org/10.1126/SCIADV.ABQ7827

Gentine, P., Entekhabi, D., Chehbouni, A., Boulet, G., & Duchemin, B. (2007). Analysis of evaporative fraction diurnal behaviour. *Agricultural and Forest Meteorology*, 143(1), 13–29. https://doi.org/10.1016/j.agrformet.2006.11.002

Green, J. K., Konings, A. G., Alemohammad, S. H., Berry, J., Entekhabi, D., Kolassa, J., Lee, J. E., & Gentine, P. (2017). Regionally strong feedbacks between the atmosphere and terrestrial biosphere. *Nature Geoscience*, 10(6), 410–414. https://doi.org/10.1038/ngeo2957

Guerrieri, R., Belmecheri, S., Ollinger, S. V., Asbjornsen, H., Jennings, K., Xiao, J., Stocker, B. D., Martin, M., Hollinger, D. Y., Bracho-Garrillo, R., Clark, K., Dore, S., Kolb, T., William Munger, J., Novick, K., & Richardson, A. D. (2019). Disentangling the role of photosynthesis and stomatal conductance on rising forest water-use efficiency. *Proceedings of the National Academy of Sciences of the United States of America*, 116(34), 16909–16914. https://doi.org/10.1073/PNAS.1905912116

Haghighi, E., Short Gianotti, D. J., Akbar, R., Salvucci, G. D., & Entekhabi, D. (2018). Soil and atmospheric controls on the land surface energy balance: A generalized framework for distinguishing moisture-limited and energy-limited evaporation regimes. *Water Resources Research*, 54(3), 1831–1851. https://doi.org/10.1002/2017WR021729

Harrison, S. P., Cramer, W., Franklin, O., Prentice, I. C., Wang, H., Brännström, Å., de Boer, H., Dieckmann, U., Joshi, J., Keenan, T. F., Lavergne, A., Manzoni, S., Mengoli, G., Morfopoulos, C., Peñuelas, J., Pietsch, S., Rebel, K. T., Ryu, Y., Smith, N. G., ... Wright, I. J. (2021). Eco-evolutionary optimality as a means to improve vegetation and

land-surface models. *New Phytologist*, 231(6), 2125–2141. https://doi.org/10.1111/NPH.17558

Hong, T., Dong, W., Ji, D., Dai, T., Yang, S., & Wei, T. (2019). The response of vegetation to rising CO_2 concentrations plays an important role in future changes in the hydrological cycle. *Theoretical and Applied Climatology*, 136(1–2), 135–144. https://doi.org/10.1007/s00704-018-2476-7

Humphrey, V., Berg, A., Ciais, P., Gentine, P., Jung, M., Reichstein, M., Seneviratne, S. I., & Frankenberg, C. (2021). Soil moisture–atmosphere feedback dominates land carbon uptake variability. *Nature*, 592(7852), 65–69. https://doi.org/10.1038/s41586-021-03325-5

Huxman, T. E., Smith, M. D., Fay, P. A., Knapp, A. K., Shaw, M. R., Loik, M. E., Smith, S. D., Tissue, D. T., Zak, J. C., Weltzin, J. F., Pockman, W. T., Sala, O. E., Haddad, B. M., Harte, J., Kock, G. W., Schwinning, S., Small, E. E., & Williams, D. G. (2004). Convergence across biomes to a common rain-use efficiency. *Nature*, 429, 651–654. https://doi.org/10.1038/nature02597.1

Jiao, W., Wang, L., Smith, W. K., Chang, Q., Wang, H., & D'Odorico, P. (2021). Observed increasing water constraint on vegetation growth over the last three decades. *Nature Communications*, 12(1), 1–9. https://doi.org/10.1038/s41467-021-24016-9

Joiner, J., Guanter, L., Lindstrot, R., Voigt, M., Vasilkov, A. P., Middleton, E. M., Huemmrich, K. F., Yoshida, Y., & Frankenberg, C. (2013). Global monitoring of terrestrial chlorophyll fluorescence from moderate-spectral-resolution near-infrared satellite measurements: Methodology, simulations, and application to GOME-2. *Atmospheric Measurement Techniques*, 6, 2803–2823. https://doi.org/10.5194/amt-6-2803-2013

Jonard, F., De Cannière, S., Brüggemann, N., Gentine, P., Short Gianotti, D. J., Lobet, G., Miralles, D. G., Montzka, C., Pagán, B. R., Rascher, U., & Vereecken, H. (2020). Value of sun-induced chlorophyll fluorescence for quantifying hydrological states and fluxes: Current status and challenges. *Agricultural and Forest Meteorology*, 291(June), 108088. https://doi.org/10.1016/j.agrformet.2020.108088

Jung, M., & FLUXCOM Team. (2016). *FLUXCOM (RS+METEO) global land carbon fluxes using CRUNCEP climate data.* Max Planck Institute for Biogeochemistry. https://doi.org/10.17871/FLUXCOM_RS_METEO_CRUNCEPv6_1980_2013_v1

Jung, M., Koirala, S., Weber, U., Ichii, K., Gans, F., Camps-Valls, G., Papale, D., Schwalm, C., Tramontana, G., & Reichstein, M. (2018). *FLUXCOM global land energy fluxes.* Max Planck Institute for Biogeochemistry. https://doi.org/10.17871/FLUXCOM_EnergyFluxes_v1

Jung, M., Koirala, S., Weber, U., Ichii, K., Gans, F., Camps-Valls, G., Papale, D., Schwalm, C., Tramontana, G., & Reichstein, M. (2019). The FLUXCOM ensemble of global land-atmosphere energy fluxes. *Scientific Data*, 6(1), 1–14. https://doi.org/10.1038/s41597-019-0076-8

Jung, M., Schwalm, C., Migliavacca, M., Walther, S., Camps-Valls, G., Koirala, S., Anthoni, P., Besnard, S., Bodesheim, P., Carvalhais, N., Chevallier, F., Gans, F., Goll, D. S., Haverd, V., Köhler, P., Ichii, K., Jain, A. K., Liu, J., Lombardozzi, D., … Reichstein, M. (2020). Scaling carbon fluxes from eddy covariance sites to globe: Synthesis and evaluation of the FLUXCOM approach. *Biogeosciences*, 17, 1343–1365. https://doi.org/10.5194/bg-17-1343-2020

Katul, G. G., Palmroth, S., & Oren, R. (2009). Leaf stomatal responses to vapour pressure deficit under current and CO_2-enriched atmosphere explained by the economics of gas exchange. *Plant, Cell and Environment*, 32(8), 968–979. https://doi.org/10.1111/J.1365-3040.2009.01977.X

Keenan, T. F., & Williams, C. A. (2018). The terrestrial carbon sink. *Annual Review of Environment and Resources*, 43, 219–243. https://doi.org/10.1146/ANNUREV-ENVIRON-102017-030204

Knapp, A. K., Ciais, P., & Smith, M. D. (2017). Tansley insight reconciling inconsistencies in precipitation—Productivity relationships: Implications for climate change. *New Phytologist*, 214, 41–47. https://doi.org/10.1111/nph.14381

Knauer, J., Zaehle, S., Reichstein, M., Medlyn, B. E., Forkel, M., Hagemann, S., & Werner, C. (2017). The response of ecosystem water-use efficiency to rising atmospheric CO_2 concentrations: Sensitivity and large-scale biogeochemical implications. *New Phytologist*, 213(4), 1654–1666. https://doi.org/10.1111/nph.14288

Kull, O. (2002). Acclimation of photosynthesis in canopies: Models and limitations. *Oecologia*, 133(3), 267–279. https://doi.org/10.1007/S00442-002-1042-1/METRICS

Lambers, H., & Oliveira, R. S. (2019). Plant physiological ecology. In *Encyclopedia of ecology, five-volume set* (3rd ed.). Springer. https://doi.org/10.1016/B978-008045405-4.00819-3

Lavergne, A., Graven, H., De Kauwe, M. G., Keenan, T. F., Medlyn, B. E., & Prentice, I. C. (2019). Observed and modelled historical trends in the water-use efficiency of plants and ecosystems. *Global Change Biology*, 25(7), 2242–2257. https://doi.org/10.1111/GCB.14634

Lemordant, L., & Gentine, P. (2019). Vegetation response to rising CO_2 impacts extreme temperatures. *Geophysical Research Letters*, 46(3), 1383–1392. https://doi.org/10.1029/2018GL080238

Liu, L., Gudmundsson, L., Hauser, M., Qin, D., Li, S., & Seneviratne, S. I. (2020). Soil moisture dominates dryness stress on ecosystem production globally. *Nature Communications*, 11(1), 1–9. https://doi.org/10.1038/s41467-020-18631-1

Manandhar, A., Sinclair, T. R., Rufty, T. W., & Ghanem, M. E. (2017). Leaf emergence (phyllochron index) and leaf expansion response to soil drying in cowpea genotypes. *Physiologia Plantarum*, 160(2), 201–208. https://doi.org/10.1111/PPL.12544

Mathias, J. M., & Thomas, R. B. (2021). Global tree intrinsic water use efficiency is enhanced by increased atmospheric CO_2 and modulated by climate and plant functional types. *Proceedings of the National Academy of Sciences of the United States of America*, 118(7), e2014286118. https://doi.org/10.1073/PNAS.2014286118

McColl, K. A., & Rigden, A. J. (2020). Emergent simplicity of continental evapotranspiration. *Geophysical Research Letters*, 47(6), 1–11. https://doi.org/10.1029/2020GL087101

McColl, K. A., & Tang, L. I. (2023). An analytic theory of near-surface relative humidity over land. *Journal of Climate*, 1, 1213–1230. https://doi.org/10.1175/JCLI-D-23-0342.1

Mrad, A., Sevanto, S., Domec, J.-C., Liu, Y., Nakad, M., & Katul, G. (2019). A dynamic optimality principle for water use strategies explains Isohydric to Anisohydric plant responses to drought. *Frontiers in Forests and Global Change*, 2, 1–35. https://doi.org/10.3389/ffgc.2019.00049

Niinemets, Ü., Keenan, T. F., & Hallik, L. (2015). A worldwide analysis of within-canopy variations in leaf structural, chemical and physiological traits across plant functional types. *New Phytologist*, 205(3), 973–993. https://doi.org/10.1111/NPH.13096

Niu, S., Xing, X., Zhang, Z., Xia, J., Zhou, X., Song, B., Li, L., & Wan, S. (2011). Water-use efficiency in response to climate change: From leaf to ecosystem in a temperate steppe. *Global Change Biology*, 17(2), 1073–1082. https://doi.org/10.1111/J.1365-2486.2010.02280.X

Pan, Y., Jackson, R. B., Hollinger, D. Y., Phillips, O. L., Nowak, R. S., Norby, R. J., Oren, R., Reich, P. B., Lüscher, A., Mueller, K. E., Owensby, C., Birdsey, R., Hom, J., & Luo, Y. (2022). Contrasting responses of woody and grassland ecosystems to increased CO_2 as water supply varies. *Nature Ecology & Evolution*, 6(3), 315–323. https://doi.org/10.1038/s41559-021-01642-6

Pappas, C., Mahecha, M. D., Frank, D. C., Babst, F., & Koutsoyiannis, D. (2017). Ecosystem functioning is enveloped by hydrometeorological variability. *Nature Ecology & Evolution*, 1(9), 1263–1270. https://doi.org/10.1038/s41559-017-0277-5

Pastorello, G., Trotta, C., Canfora, E., Chu, H., Christianson, D., Cheah, Y.-W., Poindexter, C., Chen, J., Elbashandy, A., Humphrey, M., Isaac, P., Polidori, D., Reichstein, M., Ribeca, A., van Ingen, C., Vuichard, N., Zhang, L., Amiro, B., Ammann, C., … Papale, D. (2020). The FLUXNET2015 dataset and the ONEFlux processing pipeline for

eddy covariance data. *Scientific Data 2020*, 7(1), 1–27. https://doi.org/10.1038/s41597-020-0534-3

Peñuelas, J., Ciais, P., Canadell, J. G., Janssens, I. A., Fernández-Martínez, M., Carnicer, J., Obersteiner, M., Piao, S., Vautard, R., & Sardans, J. (2017). Shifting from a fertilization-dominated to a warming-dominated period. *Nature Ecology & Evolution*, 1(10), 1438–1445. https://doi.org/10.1038/s41559-017-0274-8

Peters, W., van der Velde, I. R., van Schaik, E., Miller, J. B., Ciais, P., Duarte, H. F., van der Laan-Luijkx, I. T., van der Molen, M. K., Scholze, M., Schaefer, K., Vidale, P. L., Verhoef, A., Wårlind, D., Zhu, D., Tans, P. P., Vaughn, B., & White, J. W. C. (2018). Increased water-use efficiency and reduced CO_2 uptake by plants during droughts at a continental scale. *Nature Geoscience*, 11(10), 744–748. https://doi.org/10.1038/s41561-018-0212-7

Peterson, T. J., Saft, M., Peel, M. C., & John, A. (2021). Watersheds may not recover from drought. *Science*, 372(6543), 745–749. https://doi.org/10.1126/science.abd5085

Piao, S., Wang, X., Park, T., Chen, C., Lian, X., He, Y., Bjerke, J. W., Chen, A., Ciais, P., Tømmervik, H., Nemani, R. R., & Myneni, R. B. (2020). Characteristics, drivers and feedbacks of global greening. *Nature Reviews Earth and Environment*, 1(1), 14–27. https://doi.org/10.1038/s43017-019-0001-x

Piao, S., Wang, X., Wang, K., Li, X., Bastos, A., Canadell, J. G., Ciais, P., Friedlingstein, P., & Sitch, S. (2020). Interannual variation of terrestrial carbon cycle: Issues and perspectives. *Global Change Biology*, 26(1), 300–318. https://doi.org/10.1111/GCB.14884

Post, A. K., & Knapp, A. K. (2019). Plant growth and aboveground production respond differently to late-season deluges in a semi-arid grassland. *Oecologia*, 191, 673–683. https://doi.org/10.1007/s00442-019-04515-9

Potkay, A., & Feng, X. (2023). Dynamically optimizing stomatal conductance for maximum turgor-driven growth over diel and seasonal cycles. *AoB Plants*, 15(5), 1–16. https://doi.org/10.1093/AOBPLA/PLAD044

Reichstein, M., Stoy, P. C., Desai, A. R., Lasslop, G., & Richardson, A. D. (2012). Partitioning of net fluxes. In *Eddy covariance* (pp. 263–289). https://doi.org/10.1007/978-94-007-2351-1_9

Reynolds, J. F., & Chen, J. (1996). Modelling whole-plant allocation in relation to carbon and nitrogen supply: Coordination versus optimization: Opinion. *Plant and Soil*, 185(1), 65–74. https://doi.org/10.1007/BF02257565

Richardson, A. D., Keenan, T. F., Migliavacca, M., Ryu, Y., Sonnentag, O., & Toomey, M. (2013). Climate change, phenology, and phenological control of vegetation feedbacks to the climate system. *Agricultural and Forest Meteorology*, 169, 156–173. https://doi.org/10.1016/J.AGRFORMET.2012.09.012

Rigden, A. J., & Salvucci, G. D. (2015). Evapotranspiration based on equilibrated relative humidity (ETRHEQ): Evaluation over the continental U.S. *Water Resources Research*, 51(4), 2951–2973. https://doi.org/10.1002/2014WR016072

Rigden, A. J., & Salvucci, G. D. (2017). Stomatal response to humidity and CO_2 implicated in recent decline in US evaporation. *Global Change Biology*, 23(3), 1140–1151. https://doi.org/10.1111/gcb.13439

Ruehr, N. K., Martin, J. G., & Law, B. E. (2012). Effects of water availability on carbon and water exchange in a young ponderosa pine forest: Above- and belowground responses. *Agricultural and Forest Meteorology*, 164, 136–148. https://doi.org/10.1016/J.AGRFORMET.2012.05.015

Running, S., Mu, Q., & Zhao, M. (2015). *MOD17A2H MODIS/Terra gross primary productivity 8-day L4 global 500m SIN grid V006*. NASA EOSDIS Land Processes DAAC. https://doi.org/10.5067/MODIS/MOD17A2H.006

Sage, R. F. (2020). Global change biology: A primer. *Global Change Biology*, 26(1), 3–30. https://doi.org/10.1111/GCB.14893

Salvucci, G. D., & Gentine, P. (2013). Emergent relation between surface vapor conductance and relative humidity profiles yields evaporation rates from weather data. *Proceedings of the National Academy of Sciences of the United States of America*, 110(16), 6287–6291. https://doi.org/10.1073/pnas.1215844110

Schwalm, C. R., Anderegg, W. R. L., Michalak, A. M., Fisher, J. B., Biondi, F., Koch, G., Litvak, M., Ogle, K., Shaw, J. D., Wolf, A., Huntzinger, D. N., Schaefer, K., Cook, R., Wei, Y., Fang, Y., Hayes, D., Huang, M., Jain, A., & Tian, H. (2017). Global patterns of drought recovery. *Nature*, 548(7666), 202–205. https://doi.org/10.1038/nature23021

Schymanski, S. J., Roderick, M. L., & Sivapalan, M. (2015). Using an optimality model to understand medium and long-term responses of vegetation water use to elevated atmospheric CO_2 concentrations. *AoB Plants*, 7(1), 1–17. https://doi.org/10.1093/aobpla/plv060

Scott, R. L., Biederman, J. A., Hamerlynck, E. P., & Barron-Gafford, G. A. (2015). The carbon balance pivot point of southwestern U.S. semi-arid ecosystems: Insights from the 21st century drought. *Journal of Geophysical Research: Biogeosciences*, 120(12), 2612–2624. https://doi.org/10.1002/2015JG003181

Seager, R., Feldman, J., Lis, N., Ting, M., Williams, A. P., Nakamura, J., Liu, H., & Henderson, N. (2018). Whither the 100th Meridian? The Once and Future Physical and Human Geography of America's Arid–Humid Divide. Part II: The Meridian Moves East. *Earth Interactions*, 22(5), 1–24. https://doi.org/10.1175/EI-D-17-0012.1

Seager, R., Lis, N., Feldman, J., Ting, M., Park Williams, A., Nakamura, J., Liu, H., & Henderson, N. (2018). Whither the 100th Meridian? The once and future physical and human geography of America's arid–humid divide. Part I: the story so far. *Earth Interactions*, 22(5), 1–22. https://doi.org/10.1175/EI-D-17-0011.1

Seneviratne, S. I., Corti, T., Davin, E. L., Hirschi, M., Jaeger, E. B., Lehner, I., Orlowsky, B., & Teuling, A. J. (2010). Investigating soil moisture–climate interactions in a changing climate: A review. *Earth-Science Reviews*, 99(3), 125–161. https://doi.org/10.1016/j.earscirev.2010.02.004

Shekhar, A., Hörtnagl, L., Buchmann, N., & Gharun, M. (2023). Long-term changes in forest response to extreme atmospheric dryness. *Global Change Biology*, 29(18), 5379–5396. https://doi.org/10.1111/GCB.16846

Shevliakova, E., Malyshev, S., Martinez-Cano, I., Milly, P. C. D., Pacala, S. W., Ginoux, P., Dunne, K. A., Dunne, J. P., Dupuis, C., Findell, K. L., Ghannam, K., Horowitz, L. W., Knutson, T. R., Krasting, J. P., Naik, V., Phillipps, P., Zadeh, N., Yu, Y., Zeng, F., & Zeng, Y. (2024). The land component LM4.1 of the GFDL earth system model ESM4.1: Model description and characteristics of land surface climate and carbon cycling in the historical simulation. *Journal of Advances in Modeling Earth Systems*, 16(5), e2023MS003922. https://doi.org/10.1029/2023MS003922

Short Gianotti, D. J. (2024). *Processed data for Short Gianotti et al., "two sub-annual time-scales and coupling modes for terrestrial water and carbon cycles" (2024), Global Change Biology [data set]*. Zenodo. https://doi.org/10.5281/zenodo.13144427

Short Gianotti, D. J., & Entekhabi, D. (2024). Local and general patterns of terrestrial water-carbon coupling. *Geophysical Research Letters*, 51, 1–12. https://doi.org/10.1029/2024GL109625

Short Gianotti, D. J., Rigden, A. J., Salvucci, G. D., & Entekhabi, D. (2019). Satellite and station observations demonstrate water Availability's effect on continental-scale evaporative and photosynthetic land surface dynamics. *Water Resources Research*, 55(1), 540–554. https://doi.org/10.1029/2018WR023726

Smith, A., Lott, N., & Vose, R. (2011). The integrated surface database: Recent developments and partnerships. *Bulletin of the American Meteorological Society*, 92(6), 704–708. https://doi.org/10.1175/2011BAMS3015.1

Smith, N. G., Keenan, T. F., Colin Prentice, I., Wang, H., Wright, I. J., Niinemets, Ü., Crous, K. Y., Domingues, T. F., Guerrieri, R., Yoko Ishida, F., Kattge, J., Kruger, E. L., Maire, V., Rogers, A., Serbin, S. P., Tarvainen, L., Togashi, H. F., Townsend, P. A., Wang, M., … Zhou, S.

X. (2019). Global photosynthetic capacity is optimized to the environment. *Ecology Letters*, 22(3), 506–517. https://doi.org/10.1111/ele.13210

Song, L., Griffin-Nolan, R. J., Muraina, T. O., Chen, J., Te, N., Shi, Y., Whitney, K. D., Zhang, B., Yu, Q., Smith, M. D., Zuo, X., Wang, Z., Knapp, A. K., Han, X., Collins, S. L., & Luo, W. (2023). Grassland sensitivity to drought is related to functional composition across East Asia and North America. *Ecology*, e4220. https://doi.org/10.1002/ECY.4220

Stoy, P. C., El-Madany, T. S., Fisher, J. B., Gentine, P., Gerken, T., Good, S. P., Klosterhalfen, A., Liu, S., Miralles, D. G., Perez-Priego, O., Rigden, A. J., Skaggs, T. H., Wohlfahrt, G., Anderson, R. G., Coenders-Gerrits, A. M. J., Jung, M., Maes, W. H., Mammarella, I., Mauder, M., … Wolf, S. (2019). Reviews and syntheses: Turning the challenges of partitioning ecosystem evaporation and transpiration into opportunities. *Biogeosciences*, 16(19), 3747–3775. https://doi.org/10.5194/BG-16-3747-2019

Tei, S., Sugimoto, A., Yonenobu, H., Matsuura, Y., Osawa, A., Sato, H., Fujinuma, J., & Maximov, T. (2017). Tree-ring analysis and modeling approaches yield contrary response of circumboreal forest productivity to climate change. *Global Change Biology*, 23(12), 5179–5188. https://doi.org/10.1111/GCB.13780

Tramontana, G., Jung, M., Schwalm, C. R., Ichii, K., Camps-Valls, G., Ráduly, B., Reichstein, M., Arain, M. A., Cescatti, A., Kiely, G., Merbold, L., Serrano-Ortiz, P., Sickert, S., Wolf, S., & Papale, D. (2016). Predicting carbon dioxide and energy fluxes across global FLUXNET sites with regression algorithms. *Biogeosciences*, 13, 4291–4313. https://doi.org/10.5194/bg-13-4291-2016

Trugman, A. T., Medvigy, D., Mankin, J. S., & Anderegg, W. R. L. (2018). Soil moisture stress as a major driver of carbon cycle uncertainty. *Geophysical Research Letters*, 45(13), 6495–6503. https://doi.org/10.1029/2018gl078131

Ukkola, A. M., Prentice, I. C., Keenan, T. F., Van Dijk, A. I. J. M., Viney, N. R., Myneni, R. B., & Bi, J. (2016). Reduced streamflow in water-stressed climates consistent with CO_2 effects on vegetation. *Nature Climate Change*, 6(1), 75–78. https://doi.org/10.1038/nclimate2831

Walker, A. P., De Kauwe, M. G., Bastos, A., Belmecheri, S., Georgiou, K., Keeling, R. F., McMahon, S. M., Medlyn, B. E., Moore, D. J. P., Norby, R. J., Zaehle, S., Anderson-Teixeira, K. J., Battipaglia, G., Brienen, R. J. W., Cabugao, K. G., Cailleret, M., Campbell, E., Canadell, J. G., Ciais, P., … Zuidema, P. A. (2020). Integrating the evidence for a terrestrial carbon sink caused by increasing atmospheric CO_2. *New Phytologist*, 229(5), 2413. https://doi.org/10.1111/nph.16866

Yang, Y., Roderick, M. L., Zhang, S., McVicar, T. R., & Donohue, R. J. (2019). Hydrologic implications of vegetation response to elevated CO_2 in climate projections. *Nature Climate Change*, 9(1), 44–48. https://doi.org/10.1038/s41558-018-0361-0

Zhang, Y., Xiao, X., Jin, C., Dong, J., Zhou, S., Wagle, P., Joiner, J., Guanter, L., Zhang, Y., Zhang, G., Qin, Y., Wang, J., & Moore, B. (2016). Consistency between sun-induced chlorophyll fluorescence and gross primary production of vegetation in North America. *Remote Sensing of Environment*, 183, 154–169. https://doi.org/10.1016/j.rse.2016.05.015

SUPPORTING INFORMATION

Additional supporting information can be found online in the Supporting Information section at the end of this article.